Alma Mater Studiorum
Università degli Studi di Bologna

SCUOLA DI SCIENZE

Dipartimento di Chimica Industriale "Toso Montanari"

Corso di Laurea Magistrale in

Chimica Industriale

Classe LM-71 - Scienze e Tecnologie della Chimica Industriale

Synthesis and characterization of molecular electrode materials for lithium-ion batteries

Candidato:
Angelica Laurita

Relatore:
Chiar.mo Prof. Marco Giorgetti

Correlatore:
Chiar.mo Prof. Lorenzo Stievano

Anno Accademico 2017-2018

Acknowledgements

The elaboration of this thesis has been a really long, hard and complex work and I here sincerely wish to thank all the people who directly or indirectly contributed to it.
First of all I would like to express my thanks to my supervisor, professor Marco Giorgetti, for his precious support in all these years and for giving me the great chance to participate to an Erasmus + exchange. I want to thank professor Lorenzo Stievano as well, for being an invaluable help as well as a brilliant co-supervisor and colleague during this year.
Thanks to all the AIME team of the Charles Gerhardt Institute in Montpellier and all the people I worked with, for all the training opportunities I had during my stay there, and for teaching me that the scientific research should be above all a beautiful teamwork made up of collaboration and sharing of competences.
Thanks to Angelo as well for his important advices.
A special thanks is evidently due to my parents and my sisters, who always helped and supported me.
Thanks to Carlo because being at home is often harder than leaving and despite this he has always been the same beautiful person.
I would like to thank Valentina and her illuminating monthly calls, as well as all my friends, the old and the new ones. Among them, I want to thank especially Nikola and Anatole for our lunch at the "RU", French lessons and moments of pure friendship.
My greatest and last thank is due to all those people who were always there for a ginger tea in the afternoon sharing personal experiences, knowledges, music and cheer, because they have been my best supporters.

Abstract

Rechargeable Li-ion batteries (LIBs) are nowadays gaining more and more importance in the storage of clean energy deriving from renewable sources as well as in portable devices applications. Thus, new electrode materials are being studied by several research group in order to constantly improve performances of LIBs.

In this context, the aim of this thesis work was to synthesize, characterize and test cycling properties of two new cathodic materials: iron nitroprusside and its degradation product, called Fe(CN)O.

Cubic iron nitroprusside as well as Fe(CN)O were successfully co-precipitated and thence investigated by means of different techniques such as Mössbauer spectroscopy, CHN elemental analysis, ATR-FTIR and X-rays techniques (XRD, WDX and SEM-EDX).

Good cycling properties were registered for both the materials in LIBs and post-lithium systems such as Na and K-ion batteries. *In situ* analysis confirmed the hypothesis of a reversible reaction between materials and lithium ions occurring in the potential range of 1.7 - 4.2 V vs.Li^+/Li.

Contents

Abstract **v**

Contents **viii**

1 Introduction **1**

1 Lithium-ion batteries 1

2 Positive electrode materials for LIBs 4

3 Prussian Blue Analogues 7

2 Experimental part **11**

1 Synthesis 11

1.1 Iron nitroprusside 11

1.2 FeNP degradation product 11

2 Characterization 12

2.1 X-ray Diffraction (XRD) 12

2.2 Mössbauer Spectroscopy 12

2.3 Scanning Electron Microscopy (SEM) 13

2.4 X-Ray Fluorescence Spectroscopy (XRF) 13

2.5 CHNSO Elemental Analysis 14

2.6 Attenuated Total Reflection - Infrared Spectroscopy (ATR-FTIR) . 14

3 Electrochemical tests 14

4 *Operando* characterization 15

3 Results and Discussion **17**

1 Synthesis and characterization 17

2 Electrochemical tests 28

2.1 Iron Nitroprusside 28
2.2 Fe(CN)O 33
3 *Operando* characterization 34
3.1 FeNP 35
3.2 Fe(CN)O 38

4 Final remarks and future outlook 43

A Characterization methods 45
1 X-ray Diffraction (XRD) 45
2 Mössbauer Spectroscopy 47
3 X-Ray Fluorescence spectroscopy 48
4 CHNSO Elemental Analysis 49
5 Attenuated Total Reflection - Infrared Spectroscopy (ATR-FTIR) 50

Bibliography 59

List of Figures 63

List of Tables 65

Chapter 1

Introduction

1 Lithium-ion batteries

The fast world population growth combined to life modernization due to the rapid development of new technologies have brought, in last years, to a strong increase of the demand of primary energy, which has been met mainly by the combustion of fossil fuels [22].
Nevertheless, since fossil reserves are limited and exhaustible, oil price is increasing, strongly influenced by the economic and geopolitic trend. This instable situation, added to the awareness of the fuels contribution to the green-house effect, led to the development of alternative energy resources, such as nuclear power and renewable energy.
Nuclear power stations began has been developed since the 50^{ies} in many countries, with powers raising to almost 350 GW at the beginning of the 21^{st} century. Even if it is considered as a sustainable energy source that can positively reduce carbon emissions, the disposal of radioactive wastes is a still unsolved problem; moreover, this technology is not 100% sure and many security risks for environment and population still exist. Many serious accidents, in fact, have happened during the 70^{ies}, and after that, the construction of nuclear power plants have slowed down, also because of the elevated production cost [2].
Thus, renewable energies such as photovoltaic solar energy, wind power and geothermal energy have gained importance. The main drawback of such renewable sources, however, is their intrinsic intermittent character, and a difference between production and consumption periods usually exist. Therefore, the increase of the higher proportion of renewable energy in the existing energy mix is possible only by the implementation of storage sys-

tems. Such systems will then be able to store the excess of energy produced outside the consumption peaks, and to give it back when needed. Furthermore, the ongoing replacement of the transportation means fed by fossil fuels by new generations of electric cars, as well as the widespread increase of mobile devices require more and more stored energy [46].

All these developments trigger a certain need for long-life and low-cost storage systems, with high capacity and power performance as well as elevated security; the development of lithium-ion batteries (LIBs), started at eh beginning of the 90^{ies} and since then growing at an increasing pace, are located in this context.

LIBs belong to the family of accumulators, *i.e.*, rechargeable energy storage devices able to reversibly convert chemical energy into the electric one, and thus able to store electric energy provided by an external source and to give it back on demand [26]. More specifically, such devices, also called secondary batteries, are based on a reversible chemical reaction, which occurs spontaneously during the discharge, and which can be reversed during the charge by applying a current in the opposite direction. By contrast, the so-called primary batteries cannot be recharged and their useful life ends once the reactants are consumed during the discharge process [12].

LIBs were born as a solution to a safety problem observed in the preceding Li-metal batteries. In fact, in Li-metal batteries, lithium was used directly as the negative electrode material, and during the charge process, its electrodeposition occurred with the growth of metal dendrites (Figure 1.1(a)) which eventually crossed over the separator and contacted with the positive electrode, leading to shortcuts and often explosion hazards [56].

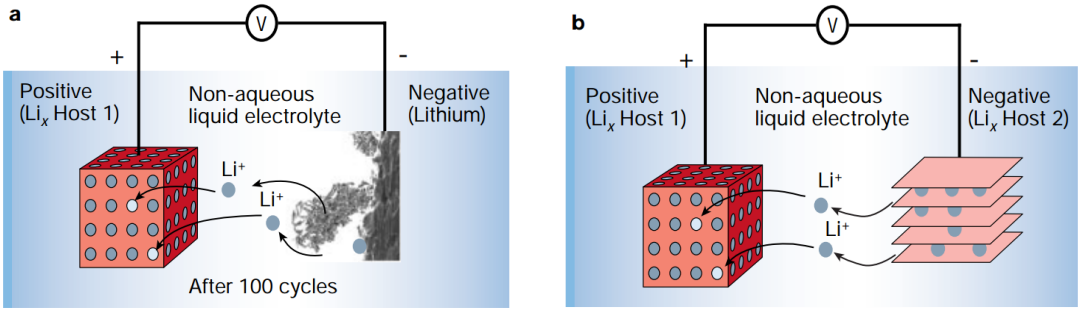

(a) Li dendritic growth.

(b) Rapresentation of the *rocking chair* system in LIBs.

Figure 1.1: Comparison between lithium-metal (a) and lithium-ion (b) batteries [56].

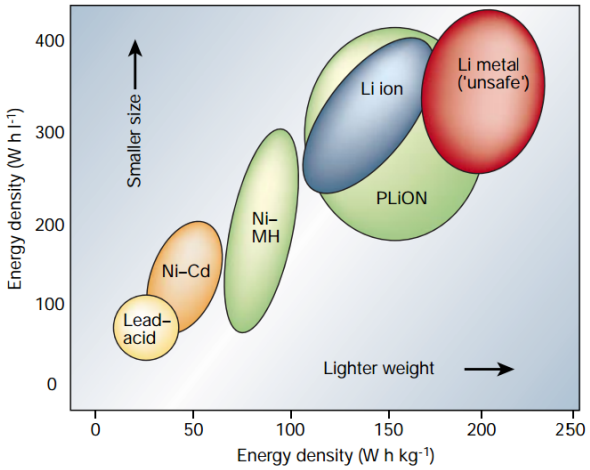

Figure 1.2: Volumetric and gravimetric energy density of the principle types of batteries [56].

To avoid this security issue, lithium metal is replaced by a different negative electrode material able to reversibly insert/deinsert lithium. In this material lithium ions are exploited as positive charges in the so called *rocking chair system* described by Goodenough and Whittingham in 1981 [40], on which LIBs are based. In LIBs, in fact, during the discharge lithium cations are simultaneously deinserted from the negative electrode and inserted in the positive one. Therefore, while the average concentration of lithium in the electrolyte remains constant during the whole process, lithium ions constantly flow from the negative electrode to the positive one, accompanied by the flow of electrons in an external circuit needed for the oxidation and the reduction of the electrode materials. During charge, the flow of electrons and lithium ions is reversed (Figure 1.1(b)).

Even if lithium metal is highly reactive, it is widely used in portable batteries because it is the most electro-positive (-3.04 V vs. SHE) and because of its lightness; these characteristics make LIBs the best technology in terms of both volumetric and gravimetric energy density, as shown in Figure 1.2.

The energy density represents the amount of electric energy deliverable by a battery per unit of volume or weight [24] and it is expressed in W·h·kg^{-1}:

$$E = \frac{C \cdot V}{m} \tag{1.1}$$

where V is the potential in Volt, m is the mass in kg and C is the nominal capacity in A·h, *i.e.*, the amount of electricity which the battery is able to deliver in fixed discharge

M^{Z+}	Abundance (%)	Price (€/ $(CO_3)^{2-}$)	Melting pt (°C)	E^0 (V*vs.*SHE)	g/mol e^-	Ionic radius (Å)	C ($mAhg^{-1}$)
Li^+	0.002	240	180	-3.04	6.941	0.68	3.8
Na^+	2.3-2.8	45	98	-2.71	22.99	1.02	1.16
K^+	2.4	12	63.5	-2.93	39.10	2.27	0.68
Mg^{2+}	2.1-2.9	40	650	-2.37	12.15	0.74	2.20

Table 1.1: Properties of principle ions for batteries.

conditions of time and current:

$$C = \int_0^t i(t)\,dt = i \cdot t \tag{1.2}$$

Similarly, the theoretical capacity can be defined as the amount of charge delivered per unit weight of active electrode material, and it is thus expressed in $A{\cdot}h{\cdot}g^{-1}$.

Lithium-based batteries have better storage ability than other battery technologies thanks to the low self-discharge rate and the absence of the so-called memory effect, which affects other types of batteries. In nickel-cadmium batteries, for example, a shallow discharge makes the battery "remember" the final discharge conditions, and a voltage drop occurs once the discharge capacity reaches the reminded value during following cycles.

In terms of applications, these characteristics make LIBs the best choice for application in portable devices as well as in electric vehicles.

However, in order to overcome the limited availability of lithium on Earth, recent researches have focused on *post-lithium* technologies, such as Na-ion, K-ion and Mg-ion batteries. Indeed, the ionic radius and the redox potential of these ions are not very different from those of lithium, as resumed in Table 1.1. For this reason, such ions can be inserted/deinserted reversibly in some materials with a mechanism very similar (but not always identical) to that of LIBs. At the same time, their abundance and their easier extraction make them a viable alternative to lithium-based systems.

2 Positive electrode materials for LIBs

Since Li^+ ions are shuttling alternatively between the positive and the negative electrode, both active electrode materials (AM) in LIBs must be able to reversibly host the lithium cations. A large variety of solids have such properties and have been tested for this ap-

plication in the last two decades, and many research group are still investigating new compounds to find out the best compromise between all the properties (capacity, working potential, cycle life, security, etc.)

Negative electrode materials can be divided into three different groups depending on the reaction mechanism with Li^+: conversion, alloy and insertion type materials.

Conversion type materials are usually binary compounds in the form M_aX_b in which M is a transition metal such as Ni, Co and Fe and X is a nonmetal *e.g.* O, S, F, N etc. During the charge, the metal is completely reduced to M^0 and lithium cations form a Li_nX matrix in which M^0 nanoparticles are encapsulated.

Alloying-type materials can be both pure metals or metal compounds such as SnO_2. the reaction with Li^+ ions proceeds in this case through a multi-step alloying mechanism, with the formation of lithiated alloys containing different amounts of Li [24].

Even if both conversion- and alloy-type materials can reach very high nominal capacities, their main drawback is the really high volume expansion (up to 200% for alloy-type materials) resulting from the strong structural modifications occurring during the reaction with lithium ions [56].

For this reason, intercalation-type materials *e.g.* the graphite are now dominating the LIBs market; since Li^+ ions are inserted inside the electrode lattice without modifying it, in fact, the volume expansion is avoided.

While negative electrode materials can react electrochemically with Li^+ via different reaction mechanisms almost all positive electrode materials work through the insertion mechanism.

During the discharge, the positive electrode (often inaccurately called "cathode", definition that works only during the discharge process) is reduced and lithium ions can be inserted inside its lattice. A distinction can be made between low voltage materials such as, *e.g.*, vanadium oxides (Figure 1.3(a)) and titanium disulfide, with working potentials in the $2 - 3.2$ V vs. $Li^+/$ range, and the nowadays more common high voltage materials.

High voltage cathode materials can be classified in three different groups depending whether the structure of the solids allows lithium diffusion via 3D, 2D or 1D channel systems:

- Layered lithium - transition metal oxides (*e.g.*, $LiCoO_2$);
- Lithium metal oxides with a spinel structure (*e.g.*;

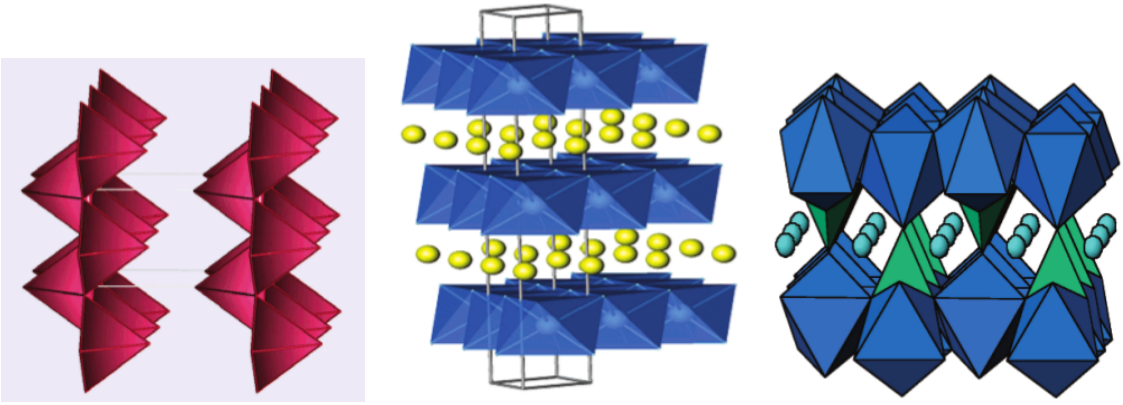

(a) Vanadium pentoxide structure. (b) Layered structure of LCO. (c) Olivine structure

Figure 1.3: Main cathodic materials structures [38].

- Lithiated polyanionic materials (*e.g.*, $LiFePO_4$).

Historically, the first cathode material used in LIBs was $LiCoO_2$, belonging to the family of the layered lithium - transition metal oxides (with general formula $Li_{(1-x)}MO_2$, with M = Co, Ni etc.). Lithium cobalt oxide (LCO)has a rock salt *fcc* structure with alternate ordered (111) layers of Li^+ and Co^{+3} cations (Figure 1.3(b)). The diffusion of Li^+ in LCO occurs with a 2D process in the Li-containing planes. During the charge process, Co^{+3} is oxidized to Co^{+4} while Li^+ ions are extracted form the structure [24].
The theoretical capacity of LCO is 274 mAh/g, corresponding to the extraction of all the lithium; however, since this material undergoes irreversible structural changes if more than 0.5 Li^+ are extracted, its practical capacity decreases to 137 mAh/g. In fact, the delithiated form of LCO forming beyond 4.1-4.2 V is not able to insert Li^+ anymore and becomes thermally instable [38, 56]. To avoid these problems and those related to the high cost and toxicity of Co, new compounds based on other transition metals have been developed. Among them, NMC compounds represent one of the best alternative to LCO, substituting it in many commercial batteries. In these materials, in fact, a part of the Co is replaced by Nichel and Manganese, reducing the material cost and toxicity and improving stability and performances [31, 32]. The high voltage spinel $LiMn_2O_4$, for example, has a comparable capacity, but Mn is not toxic and much cheaper than Co. Moreover, since manganese was previously used in alcaline batteries, recycling methods are already well-known.

As LCO, lithium manganese oxide (LMO) can be cycled in the 3-4.2V and in the past was discarded as a possible cathode material because of its low capacity at temperatures higher than 55 °C, and because of its partial solubility in the electrolyte. Despite this, many researches were done and new solutions for these drawback have been proposed.
Nowadays, new materials with an olivine ($LiMgFeSiO_4$) structure such as $LiFePO_4$ (Figure 1.3(c)) are commercialized. These compounds based on molecular ions as phosphates or sulfates are safe, low cost and non-toxic, but their energy density and voltage are relatively low.
Even if all these materials have high capacity, they are mostly known for the insertion of Li^+, and often do not work with other cations such as K^+ or Mg^{+2}. Several other families of materials, possibly exploitable in post-lithium batteries, are therefore currently studied, including molecular materials [45]. One of the most studied families of molecular cathode materials is that of Prussian Blue Analogues (PBAs). PBAs usually display a lower capacity (around 100-120 mAh/g) than the materials presented above, but are stable, cheap and very versatile, and can easily insert other cations too.

3 Prussian Blue Analogues

Prussian Blue Analogues (PBAs) are a family of active materials derived from the well-known Prussian Blue (PB), the first to be discovered. Indeed, PB, or ferric hexacyanoferrate (with formula $Fe^{III}[Fe^{II}(CN)_6]$) was accidentally synthesized for the first time by the German color-maker Heinrich Diesbach in 1706 and it is considered the first synthetic coordination compound.
Actually Diesbach, in an attempt to prepare the crimson red, accidentally added the fundamental ingredient for the synthesis of PB: the then unknown CN^- group, the real composition of which was found out only in 1814 by Joseph Louis Gay-Lussac. After this discovery, a huge number of new and modern methods for the synthesis of PB were developed. Thanks to its importance in PB structure, the cyanide group is named after the blue color of PB; indeed, the Greek word *kyaneos* means dark blue, even if the largest number of cyanides is colorless [57].
The Prussian Blue and its analogues, in fact, are characterized by a rigid cubic framework with the transition metal atoms at the edges of the cube connected by the cyano groups,

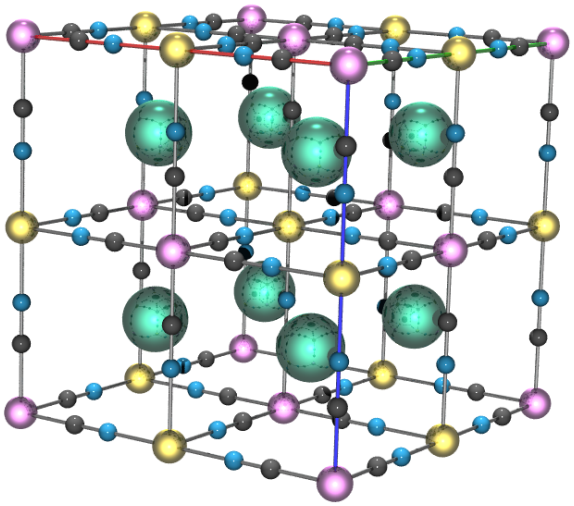

Figure 1.4: Typical PBAs structure, with green A exchangeable counterions, light blue N, gray C, pink Fe and yellow M transition metal.

forming −NC−Fe−CN−M−NC− repeating chains, as shown in Figure 1.4. Because of this typical structure in which the CN^- group links between them octahedrally coordinated sites of the metal M and of the iron forming a chain, PBAs can be considered real inorganic polymeric compounds [23].

The exchangeable counterions (A) usually occupy zeolitic interstitial positions instead; they assure the charge neutrality and, thanks to their mobility, they allow the ionic exchange which is necessary for the insertion reaction in LIBs. This regular structure is typical of the so-called *soluble* Prussian Blue, with general formula $A^{I}Fe^{III}[Fe^{II}(CN)_6] \cdot yH_2O$; depending on the preparation method, this compound can have structural defects resulting in random vacancies in the lattice. If there is the regular absence of $Fe(CN)_6$ groups, the *insoluble* PB is formed [57].

As can be seen from its general formula $(Fe_4{}^{III}[Fe^{II}(CN)_6]_3 \cdot xH_2O)$, a molecule of water is needed to fill iron vacancies in the *insoluble* PB structure. Indeed, a quarter of Fe^{II} is absent to balance charges.

Nevertheless, *soluble* and *insoluble* refer to the ability in forming colloidal solution and not to the real solubility of the compound. This property is due, in fact, to the presence of structural defects [5].

Owing to its intense blue color, PB was widely used by painters in the past, but later it found application a huge number of different fields thanks to its incredible properties.

Indeed, the PB's blue color is due to the two different oxidations states of the iron cen-

ters. By reducing both the iron atoms to Fe^{II}, a material that is named Prussian White (PW) after its color is obtained. The PW has a less regular polycrystalline structure and formula $K_4Fe_4{}^{II}[Fe^{II}(CN)_6]_3$. It is also possible to obtain the completely oxidized PB form, the *Berlin Green*, in which an anion A^- is necessary for the charge neutrality; its formula is therefore $Fe_4{}^{III}[Fe^{III}(CN)_6A]_3$ [33]. Thus, PB can reversibly change color according to the iron oxidation state through electrochemical processes. Thanks to this electrochromic disposition, that is typical of almost all PBAs, this class of materials can be used, *e.g.*, for digital displays in electronic devices [37].

Furthermore, when John F. W. Hershel accidentally noted PB's photochemical characteristics, he used began to use PB for his photographic printings. By putting potassium ferricyanide in the sunlight, in fact, the red initial material turned into the blue PB as a result of the irradiation [57].

Thanks to their previously described ability in performing ionic exchange due to their typical structure, Prussian Blue Analogues can be also used for environmental applications as the capture of heavy metal ions in aqueous solutions [36, 37, 49].

The presence of extremely reversible and electroactive redox couples in PBAs has stimulated their application in batteries as well as in sensors for a large number of ions, *e.g.*, Cs^+, K^+, Tl^+ and $NH_4{}^+$ [33].

In the last year, the Electrochemistry group of the University of Bologna has studied the use of the Copper Hexacyanoferrate in batteries as well as proposing the possible application of the Copper Nitroprusside [42, 43].

Among PBAs, the $Fe^{II}[Fe^{II}(CN)_5NO]\cdot H_2O$ (Iron Nitropusside) appears to be a really attractive material from the points of view of both application and characterization; in fact, the presence of two different Fe^{II} sites, high spin and low spin (Figure 1.5(a)), makes the Iron Nitroprusside (FeNP) very interesting to be studied by ^{57}Fe Mössbauer spectroscopy (technique described in Appendix 4). Furthermore, in addition to the electrochemical properties associated with iron redox couples, the nitrosyl group can be exploited as an electrons source since it can change its oxidation state from $(NO)^+$ to $(NO)^0$, to $(NO)^-$. For these reasons and for its PBAs typical structure able to insert and release cations, Iron Nitroprusside was synthesized in its cubic form and characterized during this internship. Actually, FeNP can present three different structures: cubic, monoclinic and orthorhombic depending on the synthesis method [25, 51]. The crystal structure as well as the hydration

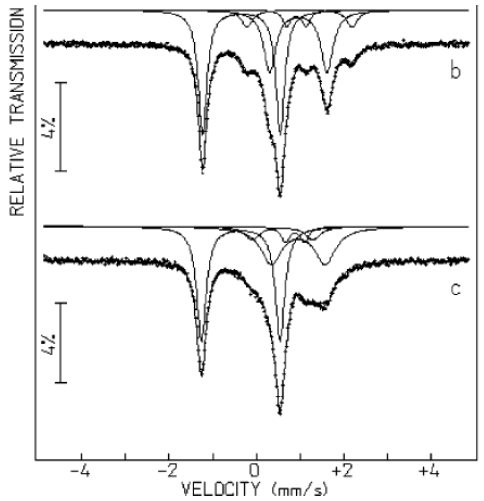

(a) Figure taken from [3]

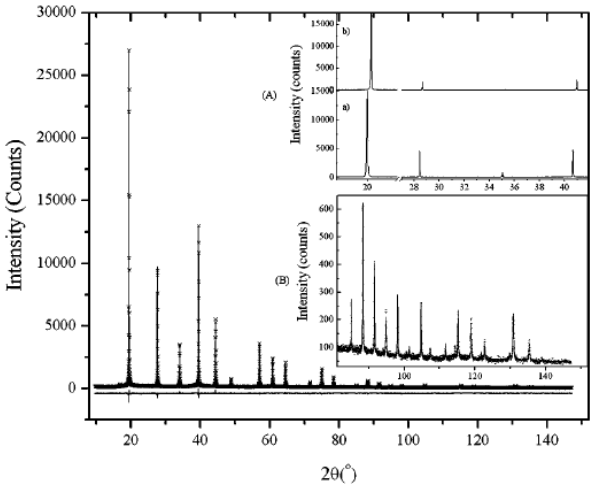

(b) Hydration effect is visible in insert A, with the dehydrated form in the top [25].

Figure 1.5: Mössbauer spectra and XRD patterns of hydrated (in the top in (a)) and dehydrated cubic Iron Nitroprusside.

degree can be determined using both XRD and Mössbauer spectroscopy. In this last, in fact, a Fe(II) contribution in the range of the low spin is always visible and independent on the amount of water and the crystalline structure; on the other hand, the high spin Fe(II) contributions can vary according to the environment of the external iron center. The X-ray diffractogram and the Mössbauer spectrum of cubic FeNP with different degree of hydration are reported in Figure 1.5.

The electrochemical properties of FeNP as a possible cathode material in LIBs and post-lithium batteries were then investigated for the first time.

Chapter 2

Experimental part

1 Synthesis

1.1 Iron nitroprusside

Iron nitroprusside (FeNP) was synthesized by co-precipitation starting from 50 mM deaerated solutions of $Na_2[Fe(CN)_5NO]$ and $(NH_4)_2Fe(SO_4)_2 \cdot 6\,H_2O$ under Argon flux. The solutions were cooled in an ice bath before mixing, and maintained at constant temperature under magnetic stirring; after mixing, the resulting solution was protected from light to avoid the photodegradation of the light-sensible nitroprusside in solution [6].
From the beginning of the drop-by-drop addition of the Mohr's Salt solution to the nitroprusside one, the red color, typical of Fe(II) complexes, turned into yellow-brownish and mat. At the end of the reaction, a brownish precipitate was clearly visible.
The powder was collected by centrifugation at 20000 rpm and 10°C for 30 minutes; subsequently it was rinsed twice with distilled water ad put to dry in the dark under vacuum. The synthesis was performed three times to test its reproducibility and samples S2 (a), S2 (b) and S2 (c) were collected (Figure 2.1(a)).

1.2 FeNP degradation product

The same synthesis was performed also using 20 mM solutions, at room temperature and under light exposition to investigate the degradation mechanism of the nitroprusside. For this purpose, after the co-precipitation, the solution was aged for two days in the sunlight and a blue-green precipitate, called Fe(CN)O (Figure 2.1(b)) was recovered by

(a) $Fe[Fe(CN)_5NO] \cdot xH_2O$. (b) Photodegradation product.

Figure 2.1: Synthesized powders.

centrifugation and dried overnight under vacuum. This synthesis was also repeated twice, and samples S1 (a) and S1 (b) were collected and studied.

2 Characterization

All the characterization techniques are described in detail in Appendix 4. Here only the experimental conditions are presented.

2.1 X-ray Diffraction (XRD)

XRD measurements were performed on all the powders to characterized them from a structural point of view. Both a X'pert PANalytical and an Empyrean diffractometers were used in the 2θ range $5° \leq 2\theta \leq 80°$ using the Cu K_α radiation ($\lambda = 1.5418$ Å). X-ray tubes of both diffractometers operated at 45kV and 30 mA.
For all the powders, the symmetry group and unit cell parameters were determined by profile matching using the computer program FullProf.

2.2 Mössbauer Spectroscopy

Transmission ^{57}Fe Mössbauer spectra were recorded at room temperature using a source of ^{57}Co(Rh) in the constant acceleration mode. A proportional counter filled with an ap-

propriate mixture of Kr and CO_2. The velocity scale was calibrated using the magnetic six line spectrum of a high-purity iron absorber. Hyperfine parameters (such as isomer shift, quadrupole splitting, full line width at half-maximum and relative resonance area) were determined by fitting the experimental data to appropriate combinations of Lorentzian lines with a nonlinear least-square method. The values of the isomer shift are given relative to $\alpha-$Fe. The spectra of the synthesized samples were measured using self-supported pellets of the appropriate thickness. *In situ* Mössbauer spectroscopy was later applied to investigate the physicochemical properties of the iron centers during discharge/charge cycles using a specifically developed *in situ* cell (see Section 4) [35].

2.3 Scanning Electron Microscopy (SEM)

SEM analyses were carried out using a Hitachi S4800 FE-SEM (voltage: 5 kV). Energy dispersive X-ray analysis (EDX) was carried out using the EDX attachment (Oxford Instruments) of the SEM system in order to study the elemental composition of individual particles of all the synthesized samples. The beam of electrons accelerated under vacuum exploited for the EDX can be in fact used in mapping configuration to study the composition and the homogeneity of the samples.

2.4 X-Ray Fluorescence Spectroscopy (XRF)

Wavelength dispersive spectrometry (WDX) was used to determine the average elemental composition of all the samples synthesized in this work. All WDX measurements were performed on an Axios XRF Spectrometer.

By combining the results of this technique with the results of EDX analyses (see Section 2.3), it was possible to calculate the empirical formula of samples, enabling to confirm the purity of iron nitroprussiate, and to identify the new compound obtained by its photodegradation in suspension.

Each sample was analyzed three times and the mean values were adopted as the real ones to calculate the generalized chemical formulas of the synthesized compounds.

2.5 CHNSO Elemental Analysis

Combustion analysis was used to determine the amount in C,H,N,O and S in all the synthesized samples, and the results were compared to those of EDX and XRF, often imprecise in the quantitative determination of light elements. The ElementarVario Micro Cube combustion analyzer used for the measurements reported in this thesis, is equipped with a proprietary Temperature Programmed Desorption (TPD) column and a Thermal Conductivity Detector (TCD). To measure the oxygen content of the samples, the combustion analysis was performed under pyrolysis conditions too.
Each sample was analyzed three times and the mean values were adopted as the real ones to calculate the generalized chemical formulas of the synthesized compounds.

2.6 Attenuated Total Reflection - Infrared Spectroscopy (ATR-FTIR)

Fourier Transform Infrared (FTIR) spectra were recorded in the 540 - 4000 cm^{-1} wavenumber range using a Nicolet Magna FTIR spectrometer equipped with an Attenuated Total Reflection (ATR) accessory. Given the significant contribution of the air components and of the diamond waveguide of the ATR accessory in the spectra, a background spectrum was registered before every measurement.

3 Electrochemical tests

The electrochemical behavior of synthesized materials was tested in the galvanostatic mode during consecutive charge/discharge cycles in a chosen potential range, versus Li metal. Since both lithium and the electrolyte are air- and moisture-sensitive, coin cell batteries were assembled in argon-filled glove box. As shown in Figure 2.2, coin cells consist in superposed layers closed by two cases mechanically sealed after filling the cell. Positive and negative electrode materials, usually casted on inert metal current collectors, are kept apart by a glass-fiber separator (Whatman GF/A) soaked with the electrolyte solution.
A disk of metallic lithium was used as the anode, while the investigated material was always at the cathode side. A 1M solution of $LiPF_6$ in a 1:1:3 mixture of ethylene carbonate (EC), propylene carbonate (PC) and dimethyl carbonate (DMC), containing 2%

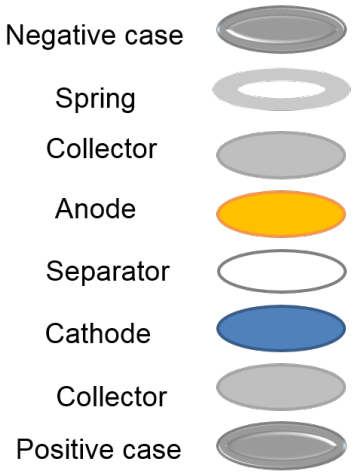

Figure 2.2: Coin cell structure.

vinylene carbonate (VC) and 5% fluoroethylene carbonate (FEC) as additives, was used as the electrolyte.

Indeed, the important role of VC in the SEI formation has already been widely investigated and supported by several researches [20, 48, 54] as well as the beneficial effect of HF derived from FEC degradation on the inhibition of dendrites formation[53]. For the cathode, different formulation were tested in order to optimize the cycling performance. Both materials were also tested in post-Lithium systems such as Na and K-ion batteries.

4 *Operando* characterization

Several of the previously presented characterization techniques were applied in the *operando* configuration, *i.e.*, by performing the measurements on the active material during discharge/charge cycles. In this way, it was possible to follow the structural and physico-chemical modifications of the electrode material during its electrochemical reaction with Li^+, thus providing vital information on the reaction mechanism. At this purpose, different *in situ* cells, each adapted to a specific characterization technique, containing electrode materials, separator and electrolyte, were used. In fact, depending on the technique, the cells are slightly different, even though their general structure is always the same (Figure 2.3). Three different parts are screwed together: the top part, the plunger and the main body. On the top part, which has a 20 mm hole, a 40 mm diameter beryllium window is placed. The cathode material is deposited on the window, with an aluminum film between them to avoid the oxidation of Be at high potential. Like in normal coin cells, a separator

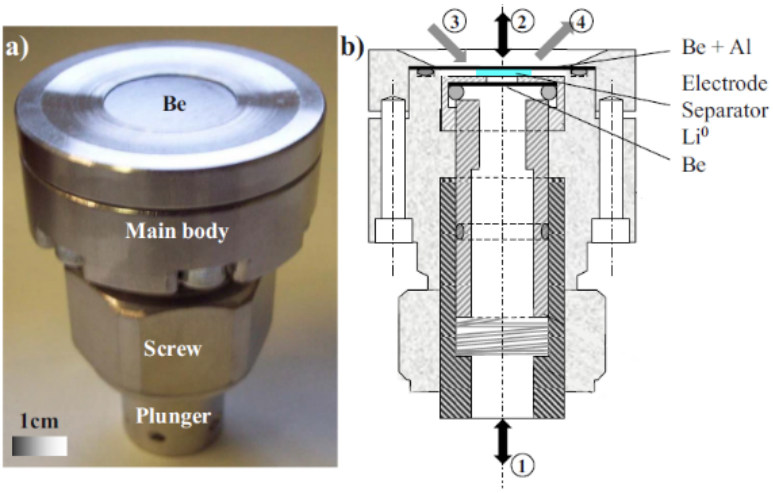

Figure 2.3: Geometry of an *in situ* cell [35].

soaked with the electrolyte in contact with the studied material keeps apart the electrode and a thin Li metal counter-electrode, which is in contact with the plunger. These components are held together by a spring pushing the plunger towards the beryllium window, to assure the correct pressure on the cell. The plunger is thus connected to the negative electrode and is separated by the positive main body by a Mylar film to avoid short-cut. The main body, in fact, is fixed to the top part by six stainless steel screws. The plunger and the main body are screwed together. To avoid air to enter in the cell, adapted gaskets and o-ring in good condition are used between the three parts.

While the main body is the same regardless of the used technique, for the measurements with transmission Mössbauer spectroscopy an additional Be window is placed on the top of an empty plunger, allowing the γ−-rays to pass through the whole cell. A full plunger is used for XRD measurements, whereas the top part of the IR *in situ* cell is replaced by the ATR sample holder.

From the electrochemical point of view, a first cycle was performed between 4.2 and 1.7 V at a C/10 rate and a second discharge until 0.5 V was done to investigate the material behavior at low potential.

The large amount of collected data was analyzed using an alternative and innovative approach, based on chemometric tools. Principal Component Analysis was used to determine the number of independent components contributing to the whole dataset, and Multivariate Curve Resolution permitted the stepwise reconstruction of the "pure" spectral components from these results.

Chapter 3

Results and Discussion

1 Synthesis and characterization

Starting from the same mother solutions, two different compounds were synthesized: FeNP and Fe(CN)O. The two compounds can be easily distinguished by their color: FeNP is a brown powder, obtained by protecting the solution from sunlight, whereas Fe(CN)O is a blue-green powder (Sample S1 (a)), and is obtained under light irradiation for two days. The difference in color reflect a substantial difference in composition and/or in the physico-chemical state of the iron centers, that can be readily probed by Mössbauer spectroscopy.

In fact, the Mössbauer spectrum of Sample S1 (a), shown in Figure 3.1, consist of a dominant quadrupole doublet with the typical hyperfine parameters of high spin Fe^{+3}. This main spectral component, which represents about 85% of the iron content of the sample as reported in Table 3.1, is accompanied by two additional doublets, represented by the blue and the orange doublets of Figure 3.1 and counting together for about 15% of the total resonance area. These two doublets are characterised by isomer shifts of -0.15(2) and 0.16(1) mm/s, typical of low spin Fe^{+2}.

These data can be compared with the spectrum of the sodium nitroprusside precursor which was also investigated by Mössbauer spectroscopy to test its purity (Figure 3.2). The spectrum of this reactant is identical to that reported in the literature for potassium nitroprusside [1], with the same structure and thus Mössbauer spectrum of NaNP, and consists of a quadrupole doublet with an isomer shift in the typical range of low-spin Fe^{+2}, indicating the absence of iron-containing decomposition products. On the other hand, by

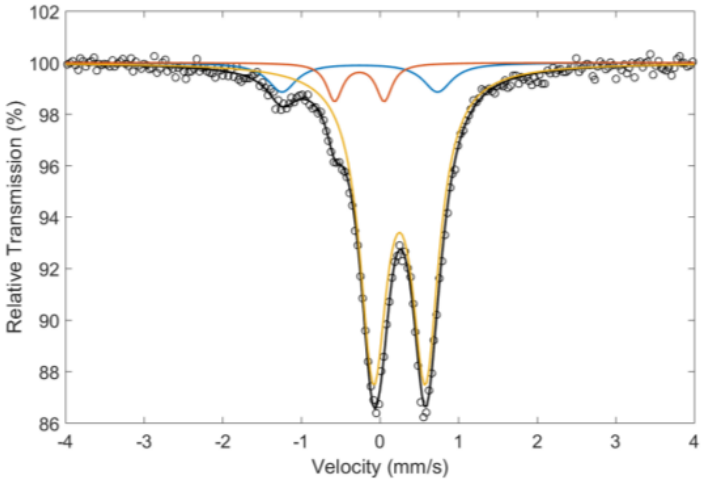

Figure 3.1: Mössbauer spectrum of the degradation product of FeNP (Sample S1 (a)).

Site	QS(mm/s)	IS(mm/s)	LW(mm/s)	Area(%)
Sample 1 (a)				
Fe(II) LS	1.98(3)	-0.15(2)	0.44(4)	9(1)
Fe(II) LS	0.63(2)	0.16(1)	0.25(3)	6(1)
Fe(III) HS	0.66(1)	0.35(1)	0.42(1)	85(1)
Sample 2 (b)				
Fe(II) LS	1.90(1)	-0.28(1)	0.30(1)	51(2)
Fe(II) HS	1.44(1)	1.11(1)	0.38(1)	36(1)
Fe(II) HS	2.62(2)	1.15(1)	0.30(4)	7(1)
Fe(II) HS	0.45(2)	1.10(2)	0.30(4)	7(1)
Sample R1				
Fe(II) LS	1.69(2)	-0.26(1)	0.25(2)	100

Table 3.1: Mössbauer parameters of the new photodegradation product, FeNP and the reactant NaNP.

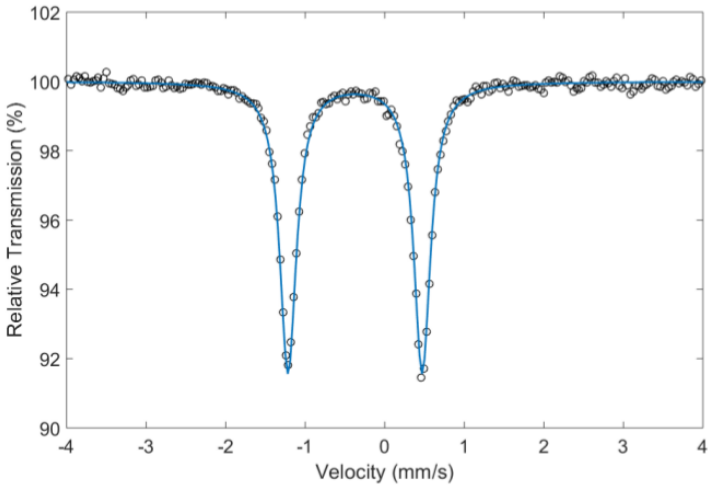

Figure 3.2: Registered Mössbauer spectrum of $Na_2[Fe(CN)_5NO] \cdot 2\,H_2O$.

comparing this spectrum with those of the FeNP samples, it is clear that they do not contain any unreacted sodium nitroprusside.

The oxidation of the iron center is probably due to the internal photoredox process between Fe^{+2}, which is oxidized to Fe^{+3}, and the NO^+ ligand, which is reduced to NO. Now, low-spin Fe^{+3} complexes are much more labile than the corresponding ones containing low-spin Fe^{+2}, facilitating the exchange of the nitrosyl and of some of the cyanide ligands with water molecules, which are present in large majority. Indeed, the exchange of strong field ligands such as cyanide with weak field ones such as water is the most probable reason for the formation of a new compound containing high-spin Fe^{+3}.

In any case, the substitution of the cyanide ligands with water molecules does not seem to be complete, since otherwise an iron oxide/hydroxide compounds would precipitate, and no blue-green iron oxide/hydroxides are known. Moreover, the observation of minor amounts of low-spin Fe^{+2} species could be associated with iron centers bonded to a larger number of cyanide ligands, in a sort of exchange equilibrium with several iron species with general formula $[Fe^{III}(CN)_n(H_2O)_{6\text{-}n}]^{+3-n}$ and a variable value of n.

The synthesis of such new compound was repeated several times, in order to obtain it in a purer form. The best condition for this synthesis were found by letting the solution in the sunlight for 48 hours (Sample S1 (b)). Even though the Mössbauer spectrum of this new sample is very similar to that of Sample S1 (a), differences were detected in the XRD patterns of the two compounds. In fact, while the analysis of Sample 1 (b) revealed a completely amorphous compound, some crystalline impurities are still present in sample

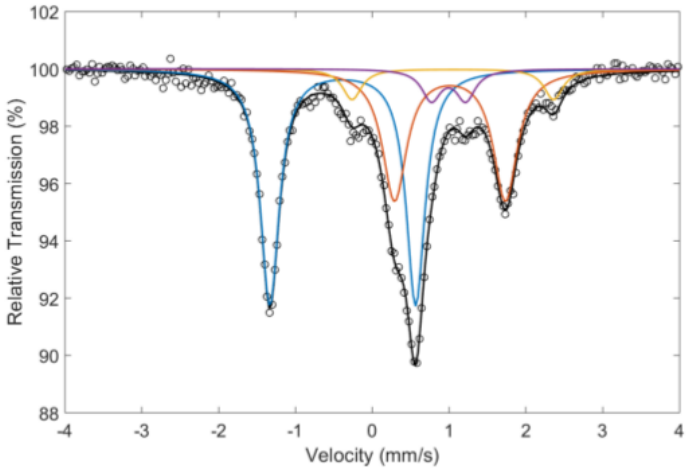

Figure 3.3: Mössbauer spectrum of Sample 2(b) (FeNP).

S1 (a).

Similarly, several different experimental conditions were tested to optimize the synthesis of the desired FeNP, in order to obtain it without impurities. The mother solutions were kept cold to maximise the precipitation of the wanted compound, and protected from sunlight as much as possible to avoid the degradation of the nitroprusside complex. Under these conditions, the preparation of different sample batches lead to very reproducible samples. All of them are in fact characterized by almost identical Mössbauer spectra, showing the presence of at least four quadrupole doublets (Figure 3.3): the dominant doublet corresponds to the starting nitroprusside unit containing low-spin Fe^{+2}, and accounts for about 50% of the total resonance area (and thus correspond to half of the iron centers). The three other doublets have very similar isomer shifts, typical of high spin Fe^{+2}, and variable quadrupole splitting, and corresponds to different local coordinations of the iron centres in the structure (iron coordinated to the nitrogen side of the cyanide groups, and to 0, 1 or 2 water molecules), as explained by Reguera *et al.* [50]. Indeed, the obtained spectra are practically identical to those shown in the literature for the cubic form of iron nitroprusside (cf. Figure 1.5(a)) [51].

In any case, no trivalent iron is contained in the different FeNP samples, confirming the suppression of the internal photo-induced electron exchange when the mother solution is protected from sunlight. Moreover, by comparing the hyperfine parameters of the different doublets of sample S2 (b) reported in Table 3.1 with those of sample S1 and of the sodium nitroprusside precursor, it is interesting to notice that no contributions from these two

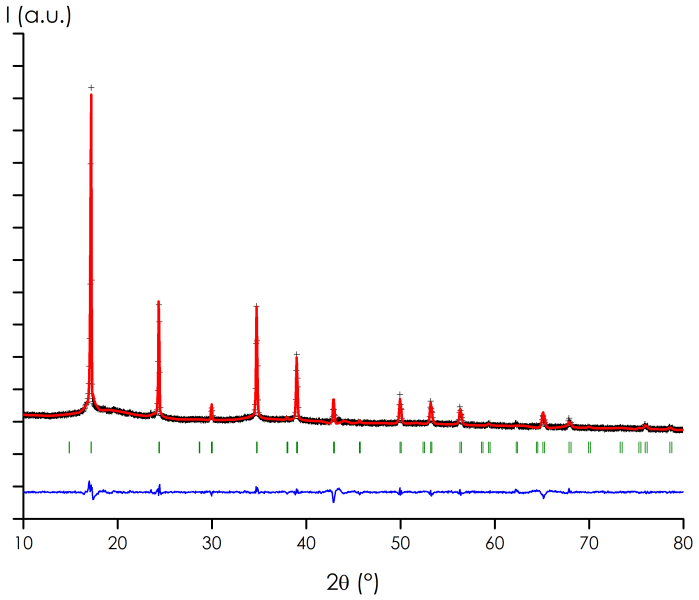

Figure 3.4: Fit and XRD pattern of FeNP (Sample 2 (c)).

compounds are visible in the spectrum of FeNP.

The three FeNP synthesized samples were also analyzed by XRD. The profile matching of the measured diffraction patterns (Figure 3.4) confirmed the presence of a single crystalline phase with a cubic $Fm-3m$ symmetry, with no noticeable crystalline impurities. The lattice parameter a was then calculated to be 10.324(1) Å, in line with previously published data (cf. Figure 1.5(b)) [25].

Well-shaped cubic crystals were also clearly visible by SEM images (Figure 3.5(a) and 3.5(b)) for all synthesized samples. However, the particle size for sample S2 (a) is slightly larger than for sample S2 (b). This difference in morphology is presumably attributed to the temperature of the synthesis. In fact, even though all the syntheses were performed with the mother solutions constantly kept in ice baths, the temperature in the laboratory changed noticeably. Therefore, sample 2 (b) was synthesized at a temperature probably higher than S2 (a), and an increase of the temperature might have induced a difference in the nucelation and growth mechanism of the particles.

The FTIR spectra of FeNP and Fe(CN)O, together with that of the reference compound sodium nitroprusside $Na_2[Fe(CN)_5NO] \cdot 2\,H_2O$, are shown in Figure 3.6. In this case, for the sake of clearness only the spectra of one sample per type of compound (sample S2 (b) for FeNP and sample S1 (a) for Fe(CN)O) are shown, since the spectra of the different

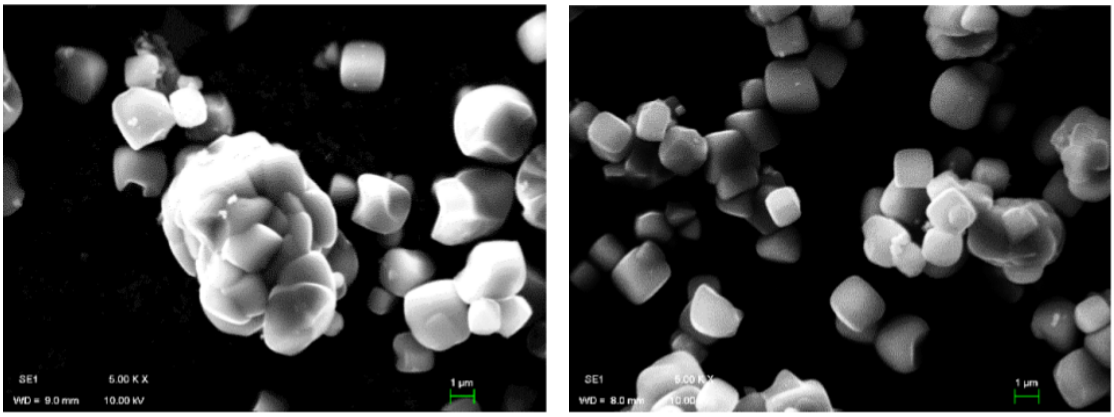

(a) S2 (a) SEM image.

(b) S2 (b) SEM image.

Figure 3.5: Temperature influence on crystals size in FeNP synthesis.

syntheses did not differ much among them. These spectra can be compared to those found in the literature [51].

In sodium nitroprusside, two strong peaks corresponding to the stretching of the NO group are expected at 1954 and 1941 cm $^{-1}$ [10]. Indeed these two peaks converge in a broad band centered at 1955 cm $^{-1}$. Similar peaks are found also in the spectra of FeNP, in agreement with the literature. In the case of Fe(CN)O, this band is also visible, even though very weak in intensity. This finding confirms the lability of the NO group caused by the photoinduced redox process at the iron center during the synthesis, as explained previously.

Similarly, the signal of the C-N stretching of pristine sodium nitroprusside is represented by a group of peaks centered at 2150 cm $^{-1}$. A similar signal, even though stronger in intensity and slightly shifted to higher wavelenght, is also found for FeNP, in full agreement with the literature ([51]). However, this is not the case for Fe(CN)O, where only a single intense band is observed around 2200 cm $^{-1}$. This observation on the one hand confirms the presence of cyanide ligands bonded to the iron center in Fe(CN)O, and on the other hand is in line with a change of the coordination sphere as well as of the oxidation/spin state of the transition metal ion in this new compound, in agreement with the results of Mössbauer spectroscopy.

In the spectrum of Fe(CN)O, an additional large band containing several contributions is visible at about 1100 cm $^{-1}$. This band resemble the typical one of sulfates, and may correspond to a small residual amount of sulfate in the powder, which let suppose that

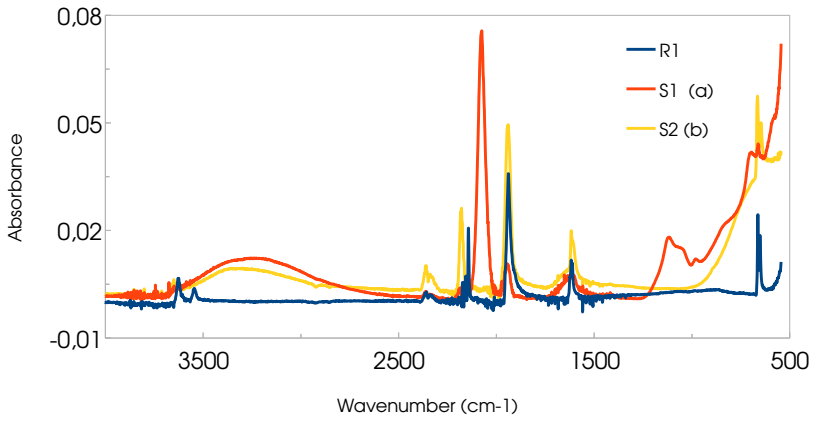

Figure 3.6: IR spectra of FeNP (sample S2 (b)), Fe(CN)O (sample S1 (a)) and of the nitroprusside precursor (noted R1).

	Technique	C/Fe	N/Fe	O/Fe	N/C
Â§	WDX	4.52	2.94	3.41	0.65
	EDX	1.05	0.75	1.60	0.71

Table 3.2: WDX and EDX data for Fe(CN)O (measured on sample S1 (a)).

the powder was probably not appropriately rinsed.

These hypotheses are supported by the elemental analyses performed on Fe(CN)O by EDX and WDX analysis. These two methods are in fact complementary: indeed, while EDX can be concentrated on single particles and/or used in mapping mode, thus providing important information on the homogeneity of the sample, WDX provides the average composition of the whole material. On the other hand, while EDX is performed under vacuum in the SEM microscope, and can therefore modify the composition of a sample containing volatile species, WDX is performed in air and should not produce modifications. By comparing the data reported in Table 3.2, carbon and nitrogen signals appear to be slightly larger in WDX analysis. These results point to the presence of partially volative CN-containing species in this compound.

The characteristic features of H_2O molecules, *i.e.*, the large band between 3000 and 3500 cm $^{-1}$ as well as the sharp one around 1560 cm $^{-1}$ are clearly visible in the spectra of both Fe(CN)O and FeNP. In the case of the different preparation batches of FeNP, the bands of water in sample S2 (a) are more pronounced than in S2 (b) and S2 (c) (Figure 3.7), suggesting an higher degree of hydration than for the other two preparations. This

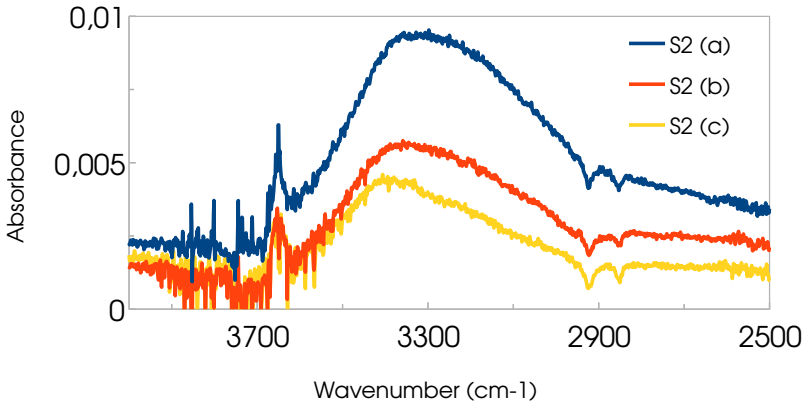

Figure 3.7: Water characteristic peak in the three FeNP samples.

result is not surprising, since differently from S2 (a), S2 (b) and S2 (c) were dried under vacuum and are thus expected to be less hydrated. To confirm this hypothesis, however, the chemical composition of the different batches was studied by combining the results of EDX, WDX and CHNS elemental analysis.

At first, the composition of different particles was analyzed by SEM-EDX in order to obtain informations about the homogeneity of the sample by comparing the results of different sampling points. For Sample 2 (b), here reported as example, the three points represented in Figure 3.8 were analyzed and compared. As it can be clearly seen from the SEM image, the sample appears homogeneous from a morphological point of view and this result is confirmed by the EDX elemental analysis reported in Table 3.3.

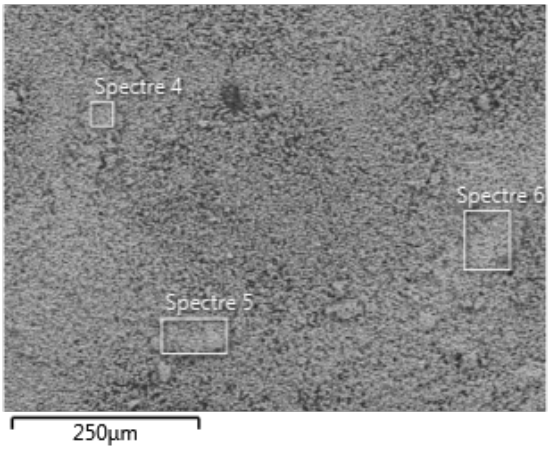

Figure 3.8: SEM image of Sample 2 (b) (FeNP) with indications on sampling points for EDX analysis.

Element	Mass %	Atomic %
Spectrum 4		
C	20.55	36.06
N	27.20	39.78
O	6.48	8.29
S	0.29	0.18
Fe	45.49	16.69
Spectrum 5		
C	20.83	35.25
N	27.15	39.41
O	6.92	8.80
S	0.43	0.27
Fe	44.67	16.26
Spectrum 6		
C	20.07	34.30
N	27.20	39.86
O	6.94	8.91
S	0.30	0.25
Fe	45.39	16.68

Table 3.3: EDX results for FeNP (Sample 2 (b)) in the sampling points indicated in Figure 3.8

Thus, since the synthesized samples composition can be considered homogeneous among sample particle, the mean elemental composition of each FeNP sample registered through EDX and WDX (Table 3.4) can be taken into account as a representative value of all the sample.

Looking at EDX data, it should also be considered that the carbon tape used as sample support could influence the measured carbon content to a different extent which depends upon the powder concentration in the analyzed point. However, EDX data are coherent with those obtained by WDX ones; in contrast with Fe(CN)O, in FeNP volatile groups are not present and IR data are thus more trustworthy. Through CHN elemental analysis it was then possible to calculate the amount of water and the general formula of compounds.

Sample	C/Fe	N/Fe	O/Fe	N/C
		EDX		
S2 (a)	2.80	2.36	0.71	0.84
S2 (b)	2.46	2.31	0.64	0.94
S2 (c)	2.11	2.35	0.50	1.11
		WDX		
S2 (a)	2.64	2.58	0.51	0.98
S2 (b)	2.51	2.42	0.57	0.96
S2 (c)	2.73	2.74	0.48	1.00

Table 3.4: FeNP EXD and WDX results for each synthesized batch.

Sample	C[%]	H[%]	N[%]	O[%]	Fe[%]
S2 (a)	15.88	2.95	23.13	26.54	30.45
S2 (b)	17.55	2.42	25.12	25.93	28.55
S2 (c)	19.02	1.65	27.29	23.07	28.78

Table 3.5: FeNP elementary analysis results.

Results for FeNP are reported in Table 3.5.

As suggested by FTIR spectra, the amount of hydrogen, from which the H_2O content was calculated, in S2 (a) is greater than in S2 (b) and S2 (c).This is undoubtedly due to different conditions in drying: S2 (b) and S2 (c) were in fact dried under vacuum and they are thus less hydrated.

The average formula for FeNP is therefore $[Fe_2(CN)_{5.27}NO_{0.72}] \cdot xH_2O$, with x depending on the drying conditions. This formula is evidently very similar to the expected one, *i.e.*, $[Fe_2(CN)_5NO_1] \cdot xH_2O$. It is interesting to notice that by summing together the number of NO^+ and CN^-, one obtains a total number of 5,99 ligands, very similar to the expected value of six ligands coordinated to the high spin iron center.

On the other hand, since the compound named Fe(CN)O was never reported in literature to the best of our knowledge, its chemical composition was harder to determine. By comparing the EDX and WDX results of samples S1 (a) and S1 (b) (Table 3.2 and Table 3.6), it appears immediately clear that the sample S1 (b) is purer, as suggested by

Technique	C/Fe	N/Fe	O/Fe	N/C
WDX	2.22	2.00	1.42	0.90
EDX	2.01	1.52	1.08	0.76

Table 3.6: FeNP (S1 (b)) WDX and EDX results.

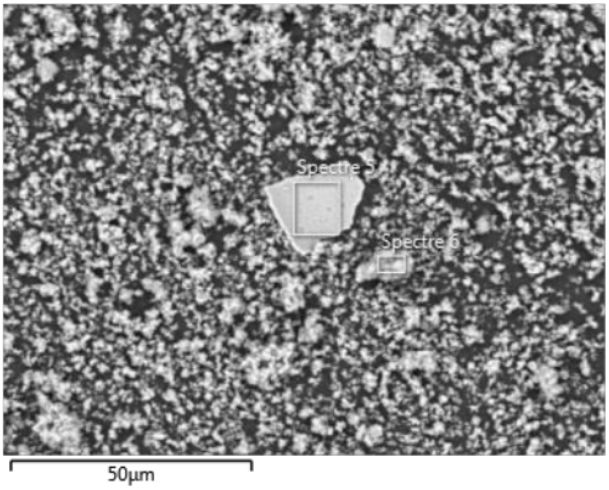

Figure 3.9: SEM image of Sample 1 (b) with indications on some sampling points for EDX analysis.

XRD analysis early in this chapter. In fact, the two XRF analyses of this sample are more similar between them than in the case of sample S1 (a).

Despite this, as it clearly appears in Figure 3.9, Sample 1 (b) is not so homogeneous neither and some compact particles are visible among the amorphous Fe(CN)O. The composition of these blocks as well as the the bulk one was investigated both using the mapping mode and concentrating the analysis on single particles.

In Figure 3.10, the results of the mapping mode composition analysis are shown. Here it is represented the superposition of different images for each element detected by the EDX analysis. Since each color is representative for an element and it appears more or less intense depending on the element concentration, it is easy to have a clear idea on the elemental composition of the sample. If we focus on one of the compact particles previously shown in Figure 3.9, such as the one in the right corner of Figure 3.9, a more intense blue color corresponding to the oxygen is clearly visible. Moreover, by analyzing single images a high concentration in sulfur and in iron is also registered, while the nitrogen and the carbon are completely absent. The presence of iron oxide and sulfates already suggested

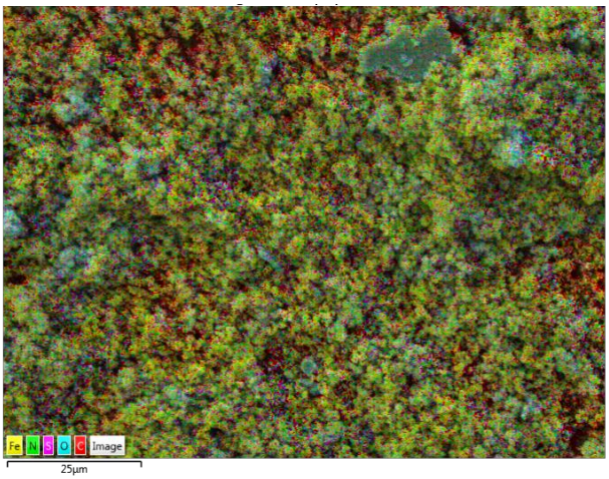

Figure 3.10: SEM-EDX image of the degradation product in Sample 1 (b). Each color is representative for an element: yellow is for Fe, green for N, pink for S, light blue for O and red for C.

by the FTIR peaks between 500 and 600 cm^{-1}, and at about 1100 cm^{-1}, respectively (cf. Figure 3.6 are thence confirmed.

In the bulk of the sample, however, the concentration of the different elements appears to be very homogeneous, allowing one to calculate the average elemental composition of the sample previously reported in Table 3.6. By considering the ratio of the light elements coming from the results of CHN elemental analysis of sample S1 (b), the best representative formula of Sample 1, which results: $Fe_2(CN)_{3.17}O_{1.93}] \cdot xH_2O$.

2 Electrochemical tests

Both FeNP and Fe(CN)O were tested in half cells versus lithium metal to investigate their electrochemical mechanism and performance. The results for the two materials will be presented in two separate sections for the sake of clarity.

2.1 Iron Nitroprusside

Since the use of Iron Nitroprusside in batteries had not been investigated yet and limited information is available in literature, the first charge/discharge cycles were carried out at different potential ranges. For this purpose, PTFE-based electrodes containing 75% of FeNP, 20% of carbon black and 5% of PTFE were mounted in coin-cells vs. lithium metal.

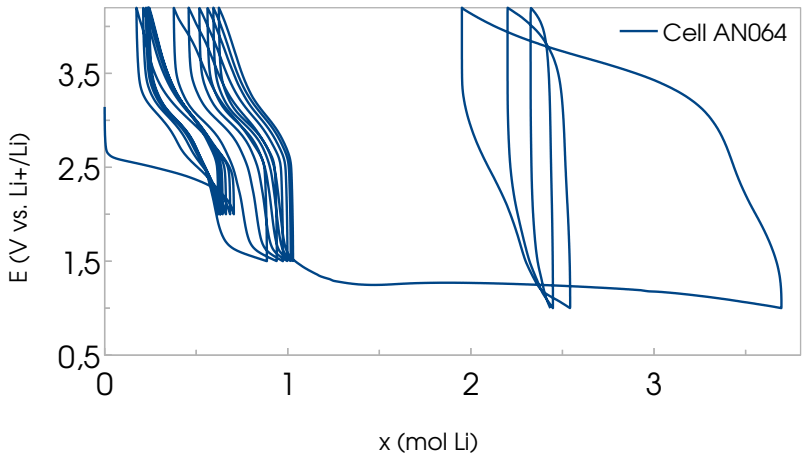

Figure 3.11: Galvanostatic cycles of FeNP in PTFE-based electrode.

Electrodes were prepared by mixing the active material (FeNP) with carbon black and PTFE in an agate mortar until a thin film was obtained. This last was then collected and dried under vacuum at 80°C overnight. Coin-cells were then assembled in the glovebox as previously explained in Chapter 2 Section 3 and tested. Since the Open Circuit Voltage (OCV) of FeNP cells was measured at 3.15 V vs. Li^+/Li, galvanostatic cycles were initially performed at a C/10 rate between 2 and 4.2 V vs. Li^0. This range was then increased by 0.5 V every five cycles to check the reversibility of the reaction at increasingly low potentials.

The galvanostatic cycles, shown in Figure 3.11, are quite reversible in the first range down to 2 V, with the insertion of about 0.5 mol of Li per mol of FeNP (calculated using the theoretical formula $Fe_2[(CN)_5NO]$) with a rather good coulombic efficiency (calculate using Equation 3.1) estimated at 97.1 % after five cycles. A similar result is found by decreasing the potential to 1.5 V, with the reaction of additional 0.5 mol of Li per mole of FeNP. When the potential is decreased to lower values, a long plateau appears around 1.3 V vs. Li^+/Li. At the end of this long plateau, a strong increase of the polarization is observed upon charge, and in the following cycles the battery capacity rapidly fades to 0 Ah/g. At a more careful analysis of the electrochemical curves, it can be seen that the long irreversible plateau starts already slightly before 1.5 V, causing a slight decrease in efficiency already during the first cycle down to 1.5 V vs. Li^+/Li. In summary, FeNP seems to cycle well at potentials above 1.7 V, whereas the irreversible reaction that occurs between 1.7 and 1.0 V vs. Li^+/Li produces a material that is not able to react electro-

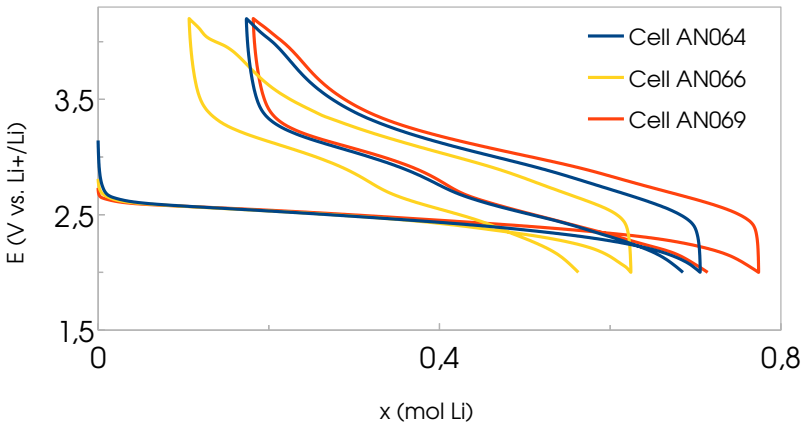

Figure 3.12: Comparison between the three synthesized active materials: S2 (a) in AN064, S2 (b) in AN066 and S2 (c) in AN069.

chemically with lithium anymore.

$$\text{Efficiency} = \left(\frac{C_{\text{charge}}}{C_{\text{discharge}}}\right) \cdot 100 \tag{3.1}$$

This same test was performed for the three synthesized FeNP batches, and practically the same behaviour was found for all of them. As an example, the first cycles for these three materials are shown in Figure 3.12. Since the electrochemical behavior of the three samples is virtually identical, in agreement with the results of their chemical characterization showing their high chemical similarity, only the tests for sample S2 (a) will be shown here.

Different formulations of FeNP electrodes, with different amounts and type of binders and carbon additives were tested in order to determine the best conditions for cycling. During these preparation, a slurry containing the active material, the carbon additive and the binder suspended/dissolved in an appropriate liquid is tape casted on the surface of a metal current collector using the Doctor Blade technique. The preparation of slurry-based electrodes is a particular critical procedure; in fact, the active material has to be well mixed with the binder and the carbon before adding an appropriate quantity of liquid. The obtained mixture has to be mechanically agitated in a ball mill for 30 minutes and spread on a collector foil using a blade of a definite height, producing a suspension film of a definite thickness (150 μm for the electrodes prepared in this work). The resulting slurry has to be as homogeneous as possible in order to obtain a uniform dispersion of the active material on the current collector; furthermore a good adherence of the slurry to the collector must be obtained. After drying, 9.5 mm diameter circular electrodes are cut out

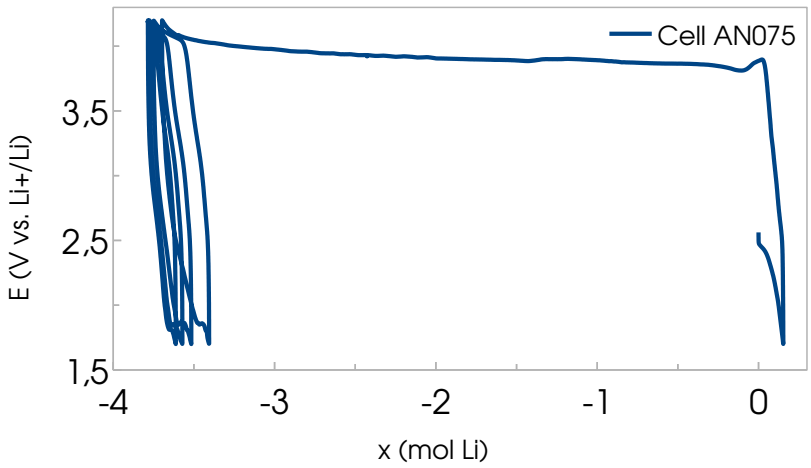

Figure 3.13: Galvanostatic cycles of FeNP in CMC-based slurry.

from the electrode film, and put to dry under vacuum at 80°C overnight. For FeNP an aluminum foil was used as the collector since copper would be oxidized during the charge process up to 4.2 V vs. Li^+/Li (the redox potential of copper in non-aqueous electrolyte is about 3.2 V vs. Li^+/Li).

A first slurry was prepared with 70% of active material, 10% of carboxymethyl cellulose (CMC), 10% of CB, 10% of vapor grounded carbon fiber (VGCF) and water as the solvent. Galvanostatic cycles were performed on several CMC-based electrodes between 1.7 and 4.2 V vs. Li^+/Li at a rate of C/10. After a normal first discharge, similar to those obtained with PTFE-based electrodes (see 3.11), a long plateau appears during the first charge between 3.8 and 4.2 V (Figure 3.13) in all the performed tests. As a consequence, the capacity begins to fall down from a starting value of 30 mAh/g to 9.5 mAh/g.

The occurring irreversible reaction was initially thought to be due to an irreversible reaction between the active material and the water possibly still present in the sample. Indeed, since the same electrolyte (1M $LiPF_6$ in EC/PC/3DMC with 2% of VC and 5% of FEC) was used for both pellet and slurry batteries, its influence in the irreversible reaction can be excluded.

Another FeNP slurry was then prepared with N-Methyl-2-pyrrolidone (NMP) instead of water and the polyvinylidene fluoride (PVDF) as binder maintaining the same mass percent as with CMC. Unfortunately, the electrochemical behavior of PVDF-based electrodes was exactly the same of CMC-based electrodes, with the very same plateau during the first charge. Other PVDF slurries were thence prepared with different amounts of solvent

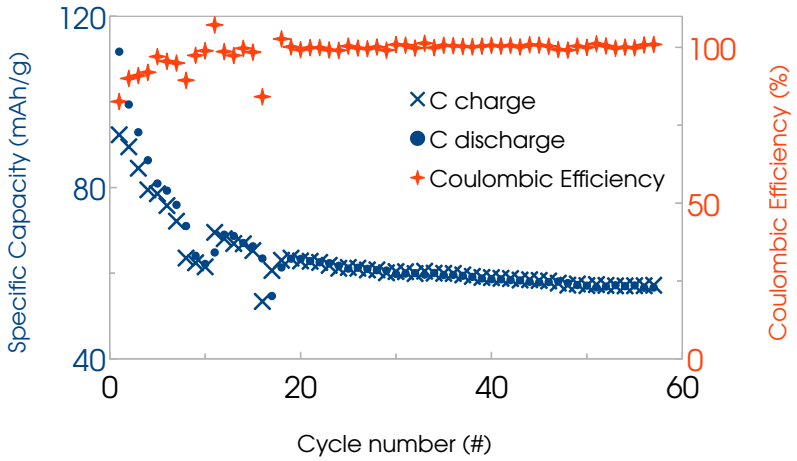

Figure 3.14: Specific Capacity and Coulombic Efficiency trends for FeNP PTFE-based electrodes vs. Li metal.

and different drying steps, but the problem could not be solved, and no appropriate cycles could be obtained starting from slurry-based electrode.

Thus, this type of electrodes were abandoned, and only new PTFE-based electrodes were prepared and cycled in batteries in order to obtain additional information on the performances of FeNP as electrode material in LIB. Using this electrode preparation method, rather reversible cycles were obtained in the previously chosen range at a C/10 rate. A significant decrease in capacity, however, occurs during the first 10 cycles; after that, the capacity is fairly stable with a small decreasing trend and steady efficiency around 100% (Figure 3.14).

Only preliminary cycing tests were conducted with FeNP electrodes versus Na and K. The obtained cycling curves are very similar to those observed with lithium, indicating that Na^+ and K^+ ions react in a similar very reversible way with FeNP (Figure 3.15); however, the obtained capacities are slightly lower than those obtained with Li, never exceeding 30 mAh/g.

The study conducted during this thesis, given the relatively short period of the internship, can be considered only as preliminary assessment of the cycling properties of FeNP. More detailed tests should therefore be conducted in order to improve its cycling performance.

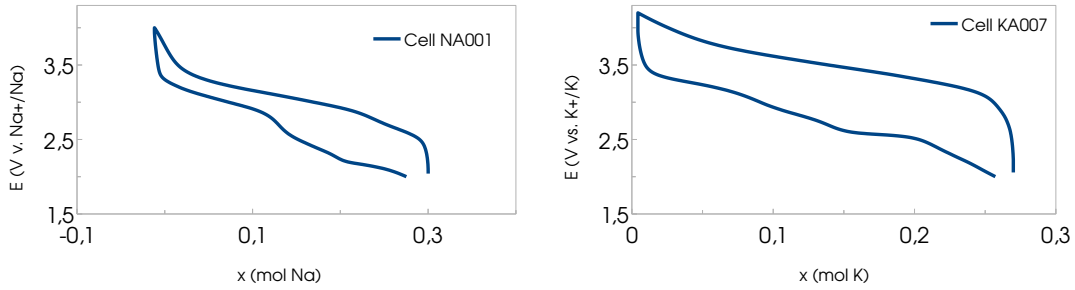

(a) Test in Na battery.

(b) Test in K battery.

Figure 3.15: Galvanostatic cycles of FeNP pellets against Sodium and Potassium.

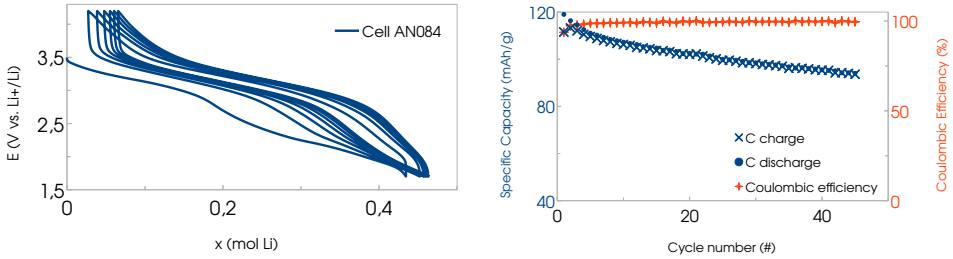

Figure 3.16: Galvanostatic cycles and corresponding performances of Fe(CN)O pellets.

2.2 Fe(CN)O

The electrochemical mechanism and performance possible Fe(CN)O in LIBs was also investigated. PTFE-based electrodes were prepared with 75% of active material and 20% of CB. With this formulation, Fe(CN)O reacts between 3.5 and 2.6 V vs. Li^+/Li in an highly reversible way; at this potential, the reduction of Fe^{3+} to Fe^{2+} is expected. A remarkable electrochemical behavior is observed in the potential range between 1.7 and 4.2 V vs. Li^+/Li at a C/10 rate (Figure 3.16(a)). In fact, if the cycling potential is maintained in this range, the specific capacity remains rather stable and higher than 100 mAh/g during the first 25 cycles, with a coulombic efficiency approaching 99% (Figure 3.16(b)). At lower potentials, however, the material undergoes an irreversible reaction and the battery performance rapidly collapses.

The same CMC and PVDF formulations used for FeNP were tested also on Sample 1 (a). Since this sample was demonstrated to be not pure, results should be interpreted keeping in mind that the pure Fe(CN)O might react in a slightly different way. From all performed tests, a peculiar behavior have to be pointed out for both the CMC and

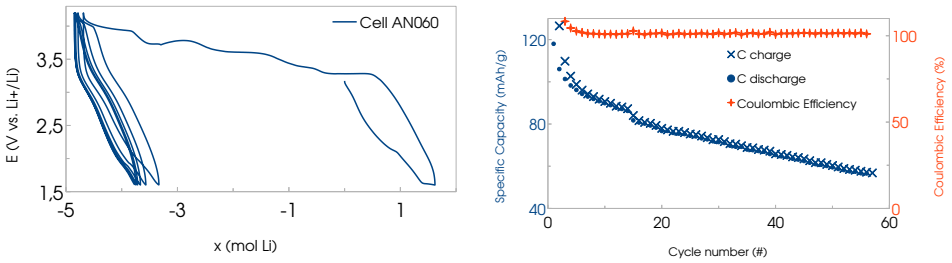

Figure 3.17: Galvanostatic cycles and corresponding performances of Fe(CN)O in CMC-based slurry.

the PVDF formulation. Even if most of the slurry-based electrodes works pretty well, in fact, a plateau similar to that of FeNP is visible in some disparate cases (Figure 3.17(a)). Despite this, the battery keeps cycling well with a beginning specific capacity of around 110 mAh/g slightly decreasing to 70 mAh/g in following cycles (Figure 3.17(b)).

However, the observed parasite reaction occurring in both FeNP and Fe(CN)O with slurry-based formulations is not necessarily the same; even if the trend of the galvanic cycle is the same for both the materials, the plateau begins at a lower potential (3.2 V vs. Li^+/Li) in Fe(CN)O than in FeNP batteries. However, purer Fe(CN)O slurry-based electrodes should also be tested in order to draw any conclusion about this reaction.

As for FeNP, some Fe(CN)O PTFE-based electrodes were tested in galvanostatic cycles also versus Na and K (Figure 3.18). Different results were obtained for the two metals. Indeed, K^+ ions does not react with the active material; on the other hand, really good cycles were obtained in sodium batteries (Figure 3.18(a)). A specific capacity of 77.2 mAh/g was obtained when cycling the material between 2 and 4 V vs. Na^0 at a C/10 rate.

3 *Operando* characterization

After the analysis of cycling properties and performance of FeNP, also its electrochemical mechanism was investigated during cycling by means of *operando* analyses. In this way, it is possible to correlate the observed electrochemical features with the physico-chemical evolution of the material during the charge/discharge cycles, as previously described in Section 4 of Chapter 2.

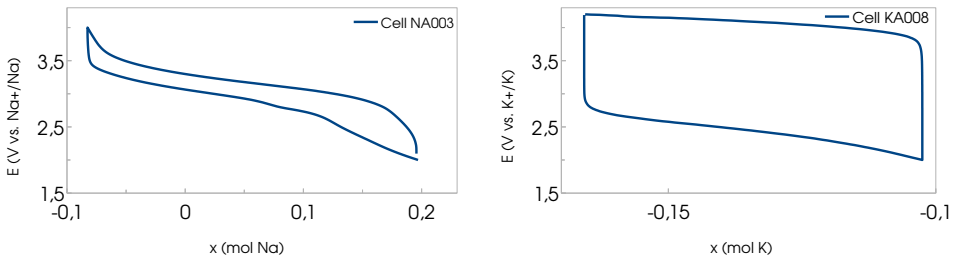

(a) Test in Na battery.

(b) Test in K battery.

Figure 3.18: Galvanostatic cycles of Fe(CN)O pellets in Sodium and Potassium batteries.

3.1 FeNP

As pointed out in the results of electrochemical tests, the electrochemical cycle of FeNP can be substantially divided into two parts: between 4.2 and 1.7 V vs. Li^+/Li a reversible reaction occurs, while beyond 1.7 V the material is irreversibly transformed in a species unable to react with Li ions anymore. Therefore, both these potential ranges were investigated by *operando* XRD in order to obtain information on the evolution of FeNP and confirmation about the involved reactions and materials. In order to study the reversibility of the mechanism, a first discharge/charge cycle was operated between 1.7 and 4.5 V vs. Li^+/Li, while the second discharge was conducted till low potentials (Figure 3.19). XRD patterns were measured continuously at constant interval of two hours in order to monitor the evolution of the electrochemical reaction.

A good and clear interpretation of *operando* results is possible only by correlating both the information in our possession (the galvanostatic cycle and XRD patterns) and it is therefore important to identify characteristic points for each process. Thus, each registered spectrum is reported on the electrochemical cycle of Figure 3.19 in yellow points, with numbers and red points to indicate diffractograms corresponding to the beginning of each important electrochemical process. The very first point corresponds to pristine FeNP, *i.e.*, the starting material before cycling. During the first two hours no current is applied and the potential of the relaxing battery is registered. The beginning of the first discharge corresponds therefore to the second diffractogram, the end of the first discharge to the 8^{th} and so on. Bearing in mind these consideration and looking at the whole XRD

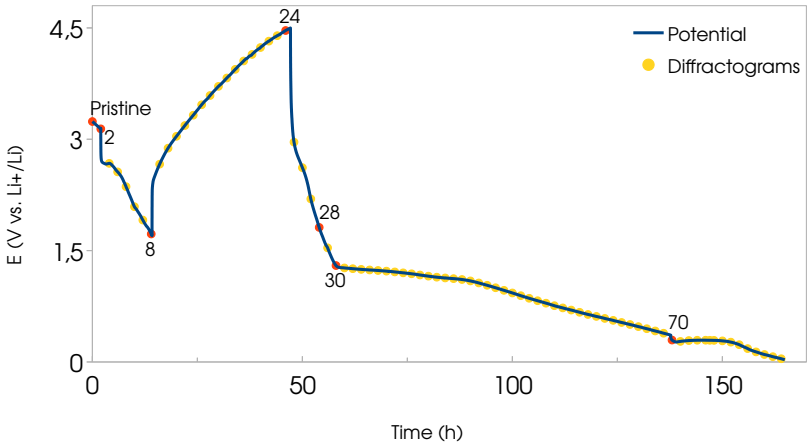

Figure 3.19: Correlation between electrochemical cycle and XRD patterns registered for FeNP during the *in situ* XRD analysis.

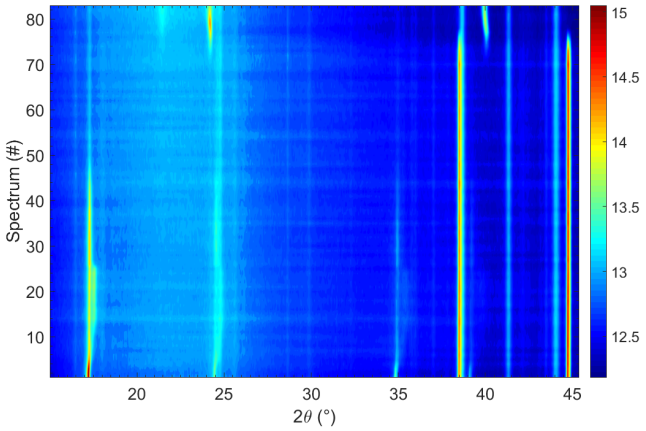

Figure 3.20: *Operando* XRD patterns of FeNP.

dataset represented in Figure 3.20 it is now possible to distinguish the development of the different electrochemical processes and analyze them in a global context.

In Figure 3.20, a cartographic view of all the registered XRD patterns is shown. The 2θ angle is represented in the abscissa, while the evolution of the patterns can be followed in the ordinate. Different colors correspond to different intensities of the peaks, going from blue (the background signal) to red (the highest peaks). From an overall point of view, important changes especially in the principal peaks at 17.5°, 24.5°, 35°and 39°are clearly visible all over the graph. Moreover, the characteristic peaks of the beryllium window of the *in situ* cell at 42°and 44°are obviously not to be taken into account in the analysis. Actually, since an aluminum foil was used in order to protect the above mentioned window, data below 0.5 V vs. Li^+/Li (pattern 70) are to consider not very representative

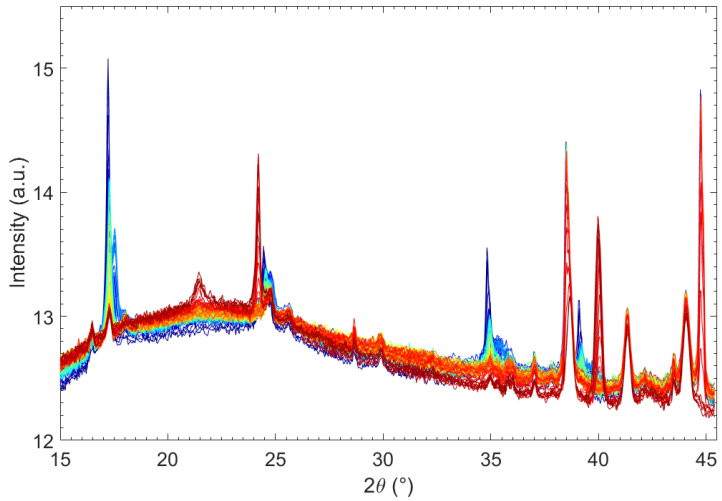

Figure 3.21: FeNP XRD patterns from a frontal view. Each color correspond to a different diffractogram, from the pristine (dark blue) to the last one (dark red).

since they are influenced by the reduction of the aluminum foil.

In addition, during the first discharge, an irreversible decrease in the intensity with a consequent broadening of all the peaks is clearly visible. After that, looking closer at the profile corresponding to the first charge and the following discharge till 1.7 V vs. Li^+/Li (pattern 28), reversible changes can be observed. All the signals result in fact to be right shifted and decreased in intensity; moreover peaks at 17.5 °and 24.5 °are split into two. Almost the same pattern of the end of the first discharge is then recovered in the 28^{th} diffractogram, as it can be clearly seen in Figure 3.21; here light blue lines that represent patterns corresponding to the end of the second discharge, understood as till 1.7 V vs. Li^+/Li, are comparable to the Pristine one, represented in dark blue, even if smaller in intensity as previously evidenced, confirming the hypothesis of a first reversible reaction in the chosen potential range. Even though it was not possible to identify exactly the phase formed at the end of the discharge, the observed reversible evolution of the peaks indicates that the initial phase is perfectly recovered at the end of the charge. The splitting of the peaks, on the other hand, indicates a modification of the space group of the pristine structure of FeNP, with a possible lowering of the symmetry. In any case, in this potential range, the material seems to work through the reversible insertion of lithium in the structure.

After that the material gradually becomes almost completely amorphous, with the still presence of small peaks clearly visible in both Figure 3.20 and 3.21. Indeed the pattern of

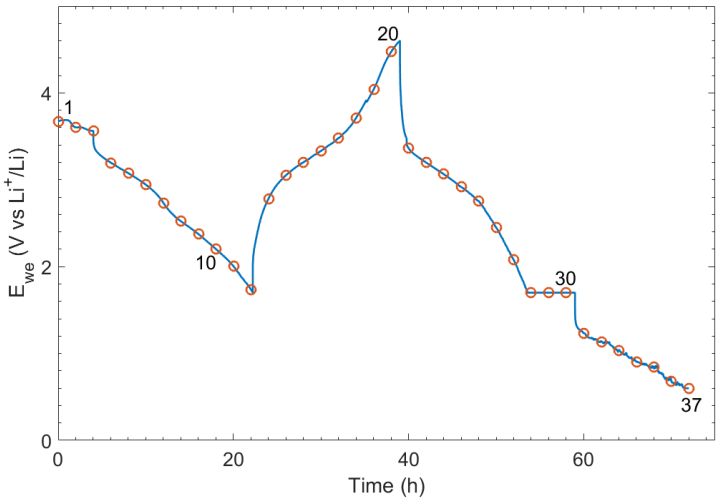

Figure 3.22: Correlation between electrochemical cycle and $_{57}$Fe Mössbauer spectra registered for Fe(CN)O during the *operando* analysis.

the residual crystalline phase, represented by dark orange and light red nuances, appears very similar to the one indicated by Reguera *et al.* [50] for the monoclinic FeNP characterized by the two peaks between 16.5°and 18°clearly visible in the registered spectra.

3.2 Fe(CN)O

In the case of Fe(CN)O, the amorphous nature of the sample unfortunately does not allow one to follow the evolution of the sample during cycling by *operando* XRD. It was therefore decided to follow its electrochemical mechanism by *operando* Mössbauer spectroscopy. In this way, it is possible to identify the evolution of the oxidation state of the iron at any point during the charge/discharge cycling. Similarly to the case of FeNP, also for Fe(CN)O cycles quite reversibly down to 1.7 V vs Li^+/Li, while after this potential the reaction becomes irreversible. Also in this case, therefore, it was decided to make the material undergo a full cycle between 4.2 and 1.7 V, and to push the second discharge down to lower potentials (0.6 V in this case).

The evolution of the electrochemical potential of the *in situ* cell during cycling is shown in Fig. 3.22, together with the number of the measured Mössbauer spectra. The first discharge stops at spectrum #12, and the first charge at spectrum #20. The second discharge finishes at spectrum #37, corresponding to a potential of 0.6 V vs. Li^+/Li.As

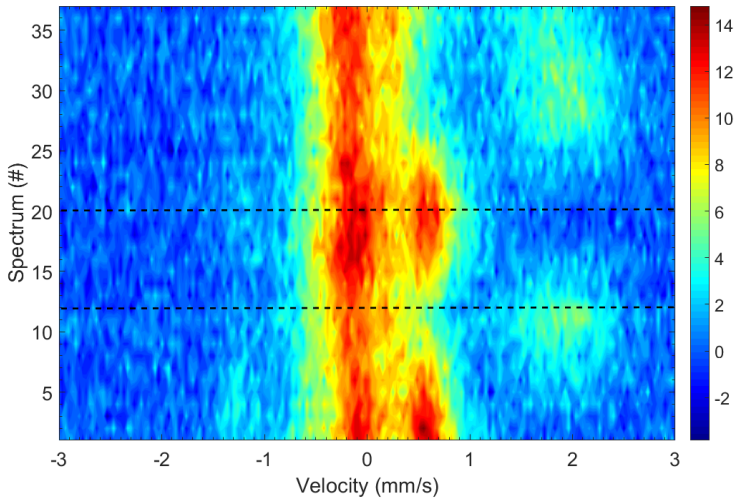

Figure 3.23: *Operando* $_{57}$Fe Mössbauer spectra of Fe(CN)O during cycling vs. Li.

for *operando* XRD, the evolution of the Mössbauer spectra is shown as a cartographic view in Fig. 3.23. The horizontal dotted lines correspond to the end of a charge or discharge process.

In order to extract the maximum valuable information from the whole series of spectra, the whole dataset was globally analyzed using a statistical method based on Principal Component Analysis (PCA) [39]. This approach is a chemometric factor analysis tool able to determine the minimal particular structures in multivariate spectral datasets. Once the number of principal components is determined by PCA, a Multivariate Curve Resolution-Alternating Least Squares (MCR-ALS) algorithm is used for the stepwise reconstruction of the pure spectral components which are necessary for interpreting the whole multiset of operando Mössbauer spectra.[18, 29, 30, 52] PCA and MCR-ALS were successfully applied to evaluate operando X-ray absorption spectroscopy and transmission X-ray microscopy data in studies of catalytic [7, 8, 28] and battery materials [4, 13, 34, 55]. In particular, it has already been applied to study battery materials by Mössbauer spectroscopy [14].
The inspection of PCA variance plot, of the shape of the principal components and of the evolution of the scores (shown respectively in Fig. 3.24(a) and 3.24(b)) shows that more than 99.3% of the variance of the whole set of Mössbauer spectra is described using the first three principal components, and that the following ones express mainly experimental noise. This number of principal component defined by PCA was then fed to the MCR-ALS algorithm. In this way, it was possible to determine the 3 pure spectra which are necessary to reconstruct the whole set of operando data. These component can now be

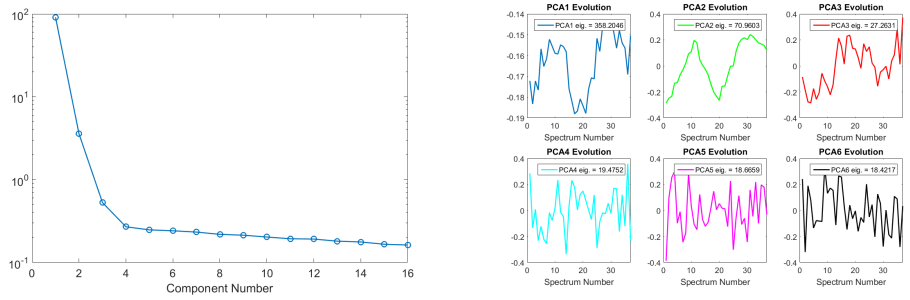

(a) Variance plot. (b) Test in K battery.

Figure 3.24: Results of the PCA analysis of the full dataset of *operando* Mössbauer spectra measured during cycling of Fe(CN)O.

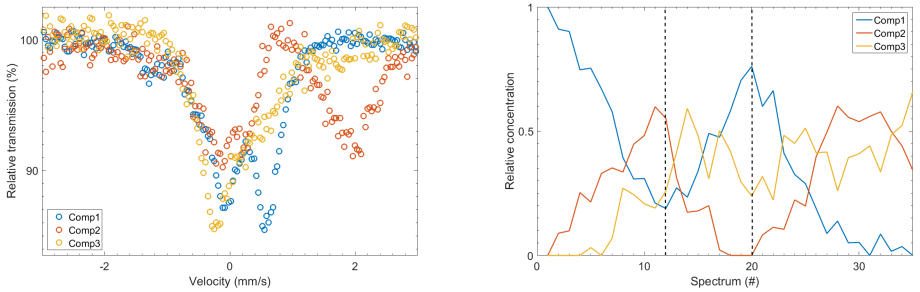

(a) MCR-ALS components (b) MCR-ALS concentrations

Figure 3.25: Pure spectral components obtained from the MCR-ALS analysis of the *operando* Mössbauer data and evolution of their concentration during cycling.

treated as normal Mössbauer spectra, and fitted in the traditional way.

The 3 reconstructed pure spectra are shown in Fig. 3.25(a) together with the evolution of their relative concentration during cycling. Their respective fit is shown in shown in Fig. 3.26, while the respective hyperfine parameters are shown in Table 3.7 Component 1 can be fitted with the same three quadrupole doublets used to fit the spectrum of pristine Fe(CN)O. It is interesting to notice that the two components relative to low spin Fe^{+2} are slightly more intense than in the spectrum of the material measured after synthesis. This modification might be due to the instability of the material in the electrolyte, with the possible reaction of structural water (bonded to the iron centers) inducing a change in local coordination.

Component 2, on the other hand, can be easily fitted using two quadrupole doublets with an isomer shift close to 1 mm/s. Such a value is typical of high spin divalent iron.

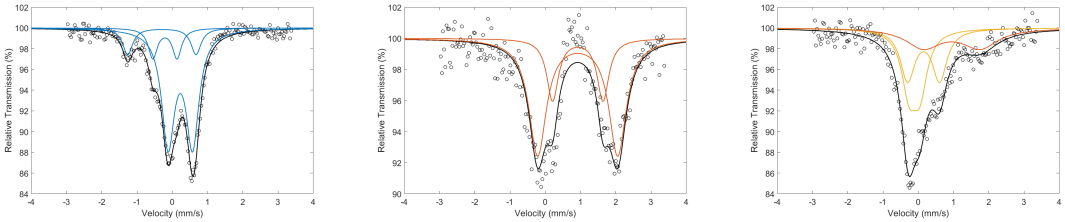

(a) MCR1 (b) MCR2 (c) MCR3

Figure 3.26: Fitting of the pure components obtained from the MCR-ALS analysis of the *operando* Mössbquer spectra.

The use of two different components reflects the multiplicity of divalent iron sites in the sample, which must be connected to different local environments.
Component 3, finally, is fitted with three different doublets with very different isomer shifts. While the weakest doublet has large values of quadrupole splitting and isomer shift, and is very similar to the divalent iron components of Component 2, the other two components are very typical of iron metal nanoparticles with sizes below 5 nm, thus undergoing superparamagnetic relaxation [17]. By putting together these results, one can

Site	QS (mm/s)	IS (mm/s)	LW (mm/s)	Area (%)
Component 1				
Fe(II) LS	1.94(9)	-0.19(5)	0.34(9)	13(4)
Fe(II) LS	0.69(5)	-0.10(4)	0.31(4)	13(4)
Fe(III) HS	0.69(2)	0.33(2)	0.44(5)	73(4)
Component 2				
Fe(II) HS	2.27(4)	1.03(2)	0.60(7)	74(5)
Fe(II) HS	1.43(5)	1.03(2)	0.60(7)	26(5)
Component 3				
Fe(O)(+Fe(III))	0.91(5)	0.25(3)	0.50(4)	33(4)
Fe(O)	0.31(6)	0.00(6)	0.50(4)	37(4)
Fe(III) HS	1.6(2)	1.05(8)	1.2(4)	3

Table 3.7: ^{57}Fe Mössbauer hyperfine parameters of the pure components obtained from the MCR-ALS analysis of the *operando* Mössbquer spectra.

try to describe the whole lithiation/delithiation cycling mechanism of Fe(CN)O:

- During the first discharge, a gradual reduction of Fe^{+3} to Fe^{+2} is observed. Towards the end of the discharge, a minor part of this divalent iron is converted to Fe metal nanoparticles. At least two different contributions of divalent iron are detected, indicating a multiplicity of different iron sites in the sample (possible differences in the coordination environment, *i.e.*, difference in type of ligands and/or distortion of the octahedral coordination.

- During the first charge, the divalent iron is oxidized back to Fe^{+3}. Interestingly, the newly formed trivalent iron has the same hyperfine parameters of pristine FeNP, indicating a perfect reversibility of the mechanism. The fraction of zerovalent iron, however, does not seem to get oxidized during charge, indicating that these iron species were irreversibly converted during the first discharge.

- After the reduction of Fe^{+3} to Fe^{+2}, the divalent iron get further reduced to iron metal nanoparticles. Since the reduction was stopped at 0.6 V vs. $Li+/Li$, however, the reduction is not yet complete, and some divalent iron is left in the sample. The trivalent iron, however, has totally disappeared at the end of the second discharge.

In summary, *operando* Mössbauer spectroscopy provides a very clear view of the reaction mechanism, indicating that only the reaction of Fe^{+3} to Fe^{+2} is reversible, and therefore the battery should be cycled only in the high voltage range to avoid the irreversible transformation of the initial compound to iron metal.

Chapter 4

Final remarks and future outlook

Iron Nitroprusside (FeNP) was successfully synthesized by co-precipitation of two equimolar solution of $Na_2[Fe(CN)_5NO] \cdot 2\,H_2O$ and $(NH_4)_2Fe(SO_4)_2 \cdot 6\,H_2O$. The synthesis was performed three times and a thorough characterization of the sample demonstrated its purity as well as a good reproducibility of the synthetic method; the general formula was calculated to be $[Fe_2(CN)_{5.27}NO_{0.72}] \cdot xH_2O$.

FeNP was tested in LIBs, and a good cycle life was obtained between in the potential range between 1.7 and 4.2 V vs. Li^+/Li when using with PTFE-based electrodes at a C/10 rate in coin-cells. In these conditions, the specific capacity resulted to be stable around 60 $mAh \cdot g^{-1}$, with a very high coulombic efficiency. Nevertheless, more tests are necessary in order to find a better electrode formulation which is able to exploit the interesting electrochemical properties of this material.

The electrochemical mechanism of FeNP in LIBs was studied by *operando* XRD. The obtained results underlined the complete reversibility of the reaction in a potential range above 1.7 V vs. Li^+/Li, where the electrochemical reaction seems to occur through an insertion mechanism.

While studying FeNP synthesis, its degradation mechanism was studied and a new interesting compound, named Fe(CN)O and containing mainly trivalent iron, was successfully synthesized and identified as $Fe_2(CN)_{3.17}O_{1.93}] \cdot xH_2O$ thanks to a thoroughgoing characterization procedure. Its electrochemical properties were investigated and this material demonstrated to react reversibly with Li^+ ions, with a specific capacity of 110 $mAh \cdot g^{-1}$, greater than FeNP.

Given its amorphous nature, the electrochemical mechanism of Fe(CN)O in LIBs could

not be studied by XRD. The use of *operando* Mössbauer spectroscopy, however, allowed us to follow the evolution of the iron species in the sample. In this case, only the reaction of Fe^{+3} to Fe^{+2}, occurring above 1.7 V vs. Li^{+}/Li was found to be reversible, whereas, at lower potentials, divalent iron is irreversibly converted to iron metal nanoparticles, causing a rapid loss of the capacity.

Appendix A

Characterization methods

1 X-ray Diffraction (XRD)

After the discovery of X-rays in 1895 by Wilhelm Conrad Röntgen, it was only in 1912 that the X-ray diffraction phenomenon is found out by Walter Friedrich, Paul Knipping and Max Laue. Initially carried out to study the X-ray's exact nature, their experiment led them to realize that, thanks to their small wavelength, X-rays could be used to investigate the inner structure of a crystal [15].
This discovery, confirmed by William Lawrance Bragg and his father, William Henry Bragg in that same year, brought to the development of the new science of X-ray crystallography [19].
X-rays are electromagnetic radiations with wavelengths in the Ångstrøm range, produced when any electrically charged particle of sufficient kinetic energy is rapidly decelerated.
When an X-ray strikes an electron (the *scatterer*) of an atom, secondary spherical waves of the same energy of the incident ones are emanated from the scatterer. This phenomenon is called elastic scattering and, in particular conditions, it can originate a diffracted beam [44].
Diffraction can be considered a scattering phenomenon in wich a large number of scattered rays are *in phase* and can produce a constructive interferce. The existance of this particular phase relation between scattered waves depends on the difference in path legth covered by the incident beam. To have a constructive interference, this difference has to be an integral multiple (represented by the reflection order n) of the wavelength of the

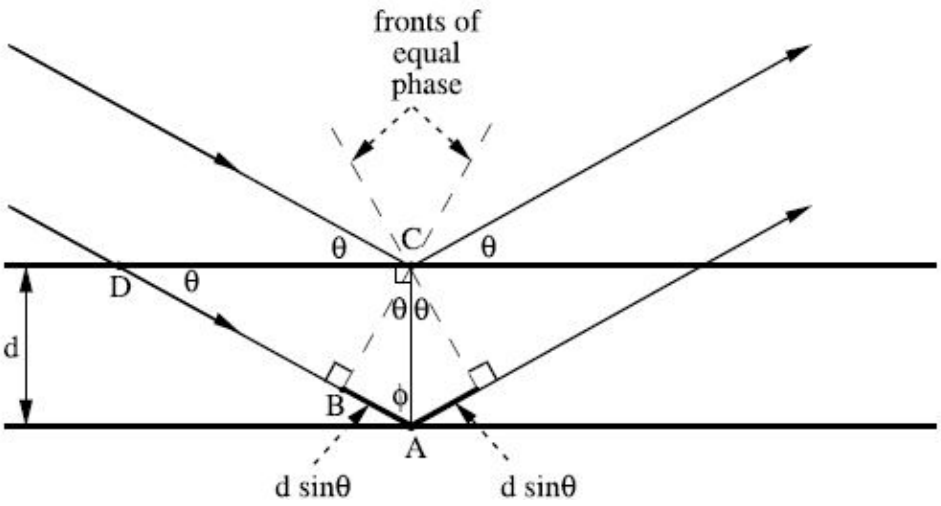

Figure A.1: Diffraction angle according to the Bragg's equation. Figure taken from [21].

incident ray (λ), as shown in the Bragg equation:

$$2\text{d } \sin\theta = n\lambda \tag{A.1}$$

where the first term is the path difference and depends on the incident angle θ, that has to be equal to the diffraction angle (Figure A.1).

If atoms are randomly arranged in the space, the scattering occurs in all directions and diffraction conditions are not present. On the other hand, if atoms are arranged in a regular lattice (like in crystals), constructive interferences occur and diffraction beams can be seen at angles that respect the Bragg law (Equation A.1). For other directions the elastic scattering is not visible, since scattered waves are added in a destructive way [15].

By measuring the intensities of the diffracted beams as a function of the angle 2θ between them and the incident X-ray, it's possible to obtain a diffraction pattern characteristic of the studied compound. In combination with the Bragg law, this diffraction pattern gives information on unit cell characteristics and atom positions in the crystal lattice. Therefore, since a long range order is necessary to see diffraction, the presence or not of narrow diffraction lines gives information about the crystal state of the analyzed sample [44].

To obtain these measurements, a movable X-rays counter is usually used as detector. As shown in Figure A.2, it rotates by the angle 2θ on a circumference centered in the powder sample, that is in the form of a flat plate and rotated at the same time by an angle θ [21].

X-rays are produced in an X-ray tube in which electrons are produced and accelerated by a potential difference. When electrons strikes the anode (or metal target), X-rays at a specific wavelength are produced because a primary scattered electrode creates a hole

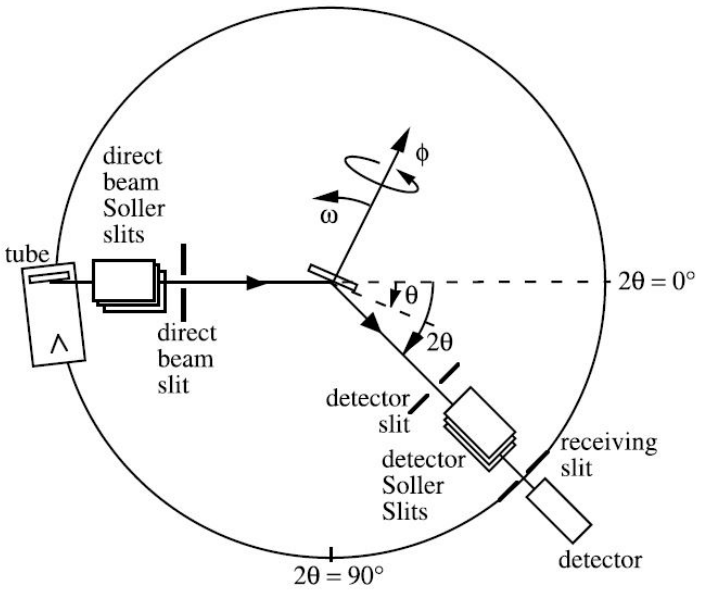

Figure A.2: Scheme of a diffractometer taken from [21]

in the K-shell that is filled by an electrode of the L-shell (in the case of a Kα line) by emitting an X-ray quantum [15].

2 Mössbauer Spectroscopy

Mössbauer Spectroscopy is a very sensitive spectroscopic technique that can provide detailed information about the physico-chemical state of atoms in a specific environment. It is based on the recoil-free nuclear resonance absorption of γ rays by a stable nucleus in an excitation transition. To have this absorption phenomenon, called Mössbauer effect and discovered by R.L. Mössbauer in 1957, the emitted γ ray is required to have the same energy needed to excite the absorber nucleus. To investigate Fe^{57}, for example, a Co^{57} γ rays source is used. This radioactive species, in fact, decays to the excited state of Fe^{57} by transforming an electron and a proton into a neutron and an electron neutrino (Electron Capture):

$$p^+ + e^- \longrightarrow n^0 + \nu_e \tag{A.2}$$

Even if the Fe^{57} produced nucleus is stable from a radioactive point of view, it is in an excited state and can decay to the ground state by emitting a γ radiation that can be absorbed by a nucleus of the same isotope, that has a natural aboundance of 2.19 %.

Furthermore, to observe the Mössbauer effect, both the sample and the source must be solid, in order to dissipate in the whole lattice the recoil momentum due to the absorption. These unwanted movements would bring to a difference in energy of $2E_R$ (with E_R recoil energy) between the source and the absorber, avoiding the absorption of the γ ray.
The energy of the nucleus also depends on its chemical environment. Since s-orbitals have a non-zero probability density in the nucleus, in fact, s-electrons can interact with the positive charge of the nucleus by Coulombic interactions of different energies depending on the electron density of external orbitals. Thus, in order to scan a proper range of energies around the resonance energy (E_0), the source is moved relatively to the absorber. When the source moves away from the sample, in fact, the wavelength λ is grater and the energy decreases, while it increase when the source is nearer to the absorber. For this reason Mössbauer spectra are usually reported in function of the velocity of the source in $mm \cdot s^{-1}$.
The electronic influence of s-electrons on the nucleus, added to the different nuclear size of the excited and the ground state, is called *Electric Monopole Interaction* and brings to a shift in the resonance line from E_0 (the *Isomer Shift* represented in Figure) given as:

$$IS = \left(\frac{c}{E_0}\right) \cdot (E_A - E_S) \tag{A.3}$$

Nuclear energy levels can also be perturbed by *Magnetic Dipole* and *Electric Quadrupole interactions*, causing different splitting of the signal due to the corresponding split of nuclear energy levels.
These three types of interactions are also called *Nuclear Hyperfine Interactions* and lead to different spectra depending on the magnetic and electronic properties (e.g. oxidation state, spin state, bonding type and site symmetry) of the investigated nucleus.

3 X-Ray Fluorescence spectroscopy

When an atom is exposed to X-rays, electrons can be expelled from inner orbitals because of the high energy of the incident radiation. These electrons create core holes in the excited atom, that can decay either by Auger emission or by X-ray fluorescence. The letter is a phenomenon that occurs when a secondary electron decays to fill the core hole

emitting an X-ray photon.[44]

The emitted radiation has an element-characteristic energy equal to the difference in energy between the two orbitals involved in the electronic transition. Since each atoms has orbitals with a characteristic energy, by measuring the energy of the fluorescence photon it's possible to identify the emitting atom, as in energy dispersive analysis (EDX).

In wavelength dispersive spectrometry (WDX), instead of measuring the energy of the emitted X-ray photon, the radiation is separated by a diffraction crystal. Since energy (E) is related to the wavelength (λ) by the Planck's constant (h) and the speed of light (c) as shown in the Planck's Law (Equation A.4), EDX and WDX analysis should be comparable.

$$\mathrm{E} = \frac{hc}{\lambda} \tag{A.4}$$

Furthermore,by measuring the intensity of each fluorescence radiation, it is possible to determine the relative quantity of the emitting element.

4 CHNSO Elemental Analysis

Combustion analysis is a method for the quantitative determination of C, H, N and S. It's based on the complete combustion of the sample in determined conditions and on the analysis of the produced oxidized compounds:

$$\mathrm{C,\ H,\ N,\ S} \xrightarrow{1050^{\circ}\mathrm{C/O_2}} \mathrm{CO_2(g) + H_2O(g) + N_2(g) + SO_2(g)} \tag{A.5}$$

Born as a gravimetric analysis [26] and used for the first time by A. Lavoisier in 1781, this method has been significantly improved in the following years [27].

Through the 18$^{\text{th}}$ and 19$^{\text{th}}$ centuries, important chemists as J. Gay-Lussac, W. Prout, J. Liebig and many others optimized the technique moving from Lavoisier's apparatus, which required 50 mg samples, to the micro-analysis method invented by F. Pregl, Nobel Prize in 1923 [16, 27].

Nowadays, the technique needs only about 2 mg of sample and, instead of weighing the combustion products, they can be analyzed by different detection methods such as thermal conductivity, infrared absorption, flame photometry and coulometry.

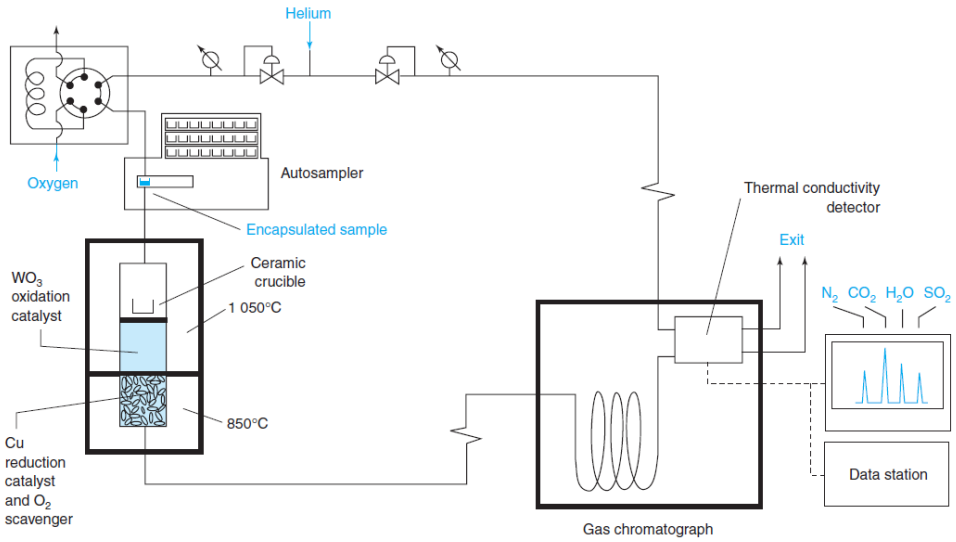

Figure A.3: C, H, N, S elemental analyzer with gas chromatograph and thermal conductivity detector [26].

Figure (A.3) represents the schema of an elemental analyzer equipped with a thermal conductivity detector, which is preceded by a gas chromatograph to separate the mixture of CO_2, H_2O, N_2 and SO_2.

The sample, after the melting of the tin sample holder, is oxidized at 1050°C in a ceramic crucible. Subsequently, hot WO_3 catalyzes the complete combustion of C to CO_2, and metallic Cu reduces all the SO_3 to SO_2.The produced mixture is then separated and detected [26].

5 Attenuated Total Reflection - Infrared Spectroscopy (ATR-FTIR)

Infrared (IR) spectroscopy exploits the the capacity of molecules to absorb radiation frequencies that match the vibrational frequencies typical of their structures. This spectroscopic technique enables, therefore, to observe different functional groups by monitoring their vibrations [9].

By IR spectroscopy it is possible to observe only vibrations that are associated with changes in the dipole moment, which depends on the variation in the electrons distribution along a bond and on its length. For two identical atoms (N_2 for example), the

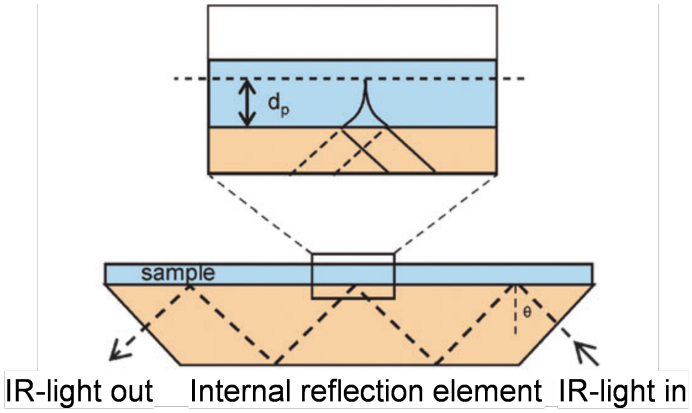

Figure A.4: ATR-FTIR principle [41].

dipole moment and its change during a stretching vibration are too small to observe an IR absorption. On the other hand, functional groups like CO,CN,NO and SO_4^{2-} are IR active [11].

ATR is a sampling technique often coupled with FTIR that enables samples to be analyzed in liquid or solid form by placing them on an Internal Reflection Element (IRE), also called waveguide.

IRE is an optical material (typically diamond or Germanium), with an higher refraction index (n_1) then the sample (n_2).

An infrared light beam is sent on the sample through the ATR crystal (Figure A.4), with an angle of incidence θ_i [41]. As shown by the Snell's law (Equation A.6), if the sinus of θ_i is greater then n_2/n_1 , there is a total internal reflection inside the IRE, since the sinus of the refracted angle (θ_r) can not be grater than 1.

$$n_1 \cdot \sin\,\theta_i = n_2 \cdot \sin\,\theta_r => \sin\,\theta_r = \frac{n_1}{n_2} \cdot \sin\,\theta_i \tag{A.6}$$

Even if the light is totally reflected, the electric field of the light penetrates inside the sample, where is absorbed and undergoes an exponential decay. This part of light is called evanescent wave, and its penetration depth (d_p) depends on the wavelength of the incident beam (λ), θ_i , n_1 and n_2:

$$d_p = \frac{\lambda/n_1}{2\pi\sqrt{\sin\,^2\theta_i - (n_2/n_1)^2}} \tag{A.7}$$

From equation A.7 it results that d_p decreases for smaller values of λ, and so does the absorbance since it is related to the optical depth (b) by the Beer-Lambert-Bouguer law:

$$A = \epsilon \cdot b \cdot c \tag{A.8}$$

where ϵ represents the molar absorptivity and c is the concentration of the absorbent species [26].

At higher λ, thus, the intensity in ATR is lower then in transmission mode and the absorbance has to be normalized for d_p.

Since d_p is usually between 0.5 and 5 μm, solid samples (like powders analyzed in this work) have to be firmly clamped against the ATR crystal [47].

Bibliography

[1] J. I. Amalvy, E. L. Varetti, and P. J. Aymonino. TGA-DTA and infrared spectra of potassium nitroprusside dihydrate: K2[Fe(CN)5NO] · 2H2O. *J. Phys. Chem. Solids*, 46(10):1153–1161, 1 1985.

[2] M. Asif and T. Muneer. Energy supply, its demand and security issues for developed and emerging economies. *Renewable and Sustainable Energy Reviews*, 11(7):1388–1413, 2007.

[3] J. Balmaseda, E. Reguera, A. Gomez, J. Roque, C. Vazquez, and M. Autie. On the Microporous Nature of Transition Metal Nitroprussides. *The Journal of Physical Chemistry B*, 107(41):11360–11369, 2003.

[4] Thibault Broux, Tahya Bamine, Laura Simonelli, Lorenzo Stievano, FranÃ§ois Fauth, Michel Ménétrier, Dany Carlier, Christian Masquelier, and Laurence Croguennec. VIV Disproportionation Upon Sodium Extraction From Na3V2(PO4)2F3 Observed by Operando X-ray Absorption Spectroscopy and Solid-State NMR. *The Journal of Physical Chemistry C*, 121(8):4103–4111, 3 2017.

[5] H. J. Buser, D. Schwarzenbach, W. Petter, and Andreas Ludi. The crystal structure of Prussian Blue: Fe4[Fe(CN)6]3.xH2O. *Inorganic Chemistry*, 16(11):2704–2710, 1977.

[6] Anthony R Butler, Joseph Mcginnis, and William I K Blsset. Further Investigation-sRegardingthe Toxicityof Sodium Nitroprusside. 492:490–492, 1987.

[7] Wellington H Cassinelli, Leandro Martins, Marina Magnani, Sandra H Pulcinelli, ValÃ©rie Briois, and Celso V Santilli. Time-resolved XAS/MS/Raman monitoring of mutual copper self-reduction and ethanol dehydrogenation reactions. *RSC Advances*, 6(25):20453–20457, 2016.

[8] Wellington H Cassinelli, Leandro Martins, Aline R Passos, Sandra H Pulcinelli, Celso V Santilli, AmÃ©lie Rochet, and ValÃ©rie Briois. Multivariate curve resolution analysis applied to time-resolved synchrotron X-ray Absorption Spectroscopy monitoring of the activation of copper alumina catalyst. *Catalysis Today*, 229:114–122, 2014.

[9] Marta Cerruti. Surface characterization of silicate bioceramics. *Philosophical Transactions of the Royal Society A: Mathematical, Physical and Engineering Sciences*, 370(1963):1281–1312, 2012.

[10] M E Chacon Villalba, J A Guida, E L Varetti, and P J Aymonino. Infrared evidence of NO linkage photoisomerization in Na2[Fe(CN)5 NO]·2H2 O at low temperature: experimental and theoretical (DFT) isotopic shifts from 15 N(O), 18 O and 54Fe species. *Spectrochimica Acta*, 57(Part A):367–373, 2001.

[11] Jonathan Clayden, Nick Greeves, Stuart Warren, and Peter Wothers. *Organic Chemistry*, volume 40. 2001.

[12] A. Vincent Colin and Bruno Scrosati. *Modern batteries. An introduction to electrochemical power sources*. 1997.

[13] Paolo Conti, Silvia Zamponi, Marco Giorgetti, Mario Berrettoni, and William H Smyrl. Multivariate Curve Resolution Analysis for Interpretation of Dynamic Cu K-Edge X-ray Absorption Spectroscopy Spectra for a Cu Doped V2O5 Lithium Battery. *Analytical Chemistry*, 82(9):3629–3635, 5 2010.

[14] GaÃ≪l Coquil, Julien Fullenwarth, Gal Grinbom, Moulay Tahar Sougrati, Lorenzo Stievano, David Zitoun, and Laure Monconduit. FeSi4P4: A novel negative electrode with atypical electrochemical mechanism for Li and Na-ion batteries. *Journal of Power Sources*, 372:196–203, 2017.

[15] B. D. Cullity. *Elements of DIFFRACTION*. 1978.

[16] Laurie Cullum and Andrew R Barron. Introduction to combustion analysis. *OpenStax-CNX*, m43578:1–8.

[17] Ali Darwiche, Matthieu Toiron, Moulay T Sougrati, Bernard Fraisse, Lorenzo Stievano, and Laure Monconduit. Performance and mechanism of FeSb2 as negative electrode for Na-ion batteries. *Journal of Power Sources*, 280:588–592, 2015.

[18] Anna de Juan, Joaquim Jaumot, and RomÃ Tauler. Multivariate Curve Resolution (MCR). Solving the mixture analysis problem. *Analytical Methods*, 6(14):4964–4976, 2014.

[19] M. Eckert. Max von Laue and the discovery of X-ray diffraction in 1912. *Annalen der Physik*, 524(5):83–85, 2012.

[20] L. El Ouatani, R. Dedryvere, C. Siret, P. Biensan, and D. Gonbeau. Effect of Vinylene Carbonate Additive in Li-Ion Batteries: Comparison of LiCoO2/C, LiFePO4/C, and LiCoO2/Li4Ti5O12 Systems. *Journal of The Electrochemical Society*, 156(6):A468–A477, 2009.

[21] Brent Fultz and James M. Howe. *Transmission Electron Microscopy and Diffractometry of Materials (Third Edition)*. 2007.

[22] Patrick Gerland, Adrian E Raftery, Hana SevcIkova, Nan Li, Danan Gu, Leontine Alkema, Bailey K Fosdick, Jennifer Chunn, Nevena Lalic, Guiomar Bay, Thomas Buettner, Gerhard K Heilig, and John Wilmoth. World Population Stabilization Unlikely This Century Patrick. *Science*, 346(6206):234–237, 2014.

[23] Marco Giorgetti. A Review on the Structural Studies of Batteries and Host Materials by X-Ray Absorption Spectroscopy. *ISRN Mater. Sci*, 2013:938625, 2013.

[24] Christian Glaize and Sylvie Geniès. *Lithium batteries and other electrochemical storage systems*. 2013.

[25] A. Gomez, J. Rodriguez-Hernandez, and E. Reguera. Crystal structures of cubic nitroprussides: M[Fe(CN)5NO]·xH2O(M=Fe, Co, Ni). Obtaining structural information from the background. *Powder Diffraction*, 22(01):27–34, 2007.

[26] Daniel C. Harris. *Quantitative chemical analysis*. 2016.

[27] Frederic L. Holmes. Elementary Analysis and the Origins of Physiological Chemistry. *Isis*, 54(1):50–81, 1963.

[28] Jingping Hong, Eric Marceau, Andrei Y Khodakov, Lucia Gaberová, Anne Griboval-Constant, Jean-SÃ©bastien Girardon, Camille La Fontaine, and ValÃ©rie Briois. Speciation of Ruthenium as a Reduction Promoter of Silica-Supported Co Catalysts: A Time-Resolved in Situ XAS Investigation. *ACS Catalysis*, 5(2):1273–1282, 2 2015.

[29] Joaquim Jaumot, Anna de Juan, and RomÃ Tauler. MCR-ALS GUI 2.0: New features and applications. *Chemometrics and Intelligent Laboratory Systems*, 140:1–12, 2015.

[30] Joaquim Jaumot, Raimundo Gargallo, Anna de Juan, and RomÃ Tauler. A graphical user-friendly interface for MCR-ALS: a new tool for multivariate curve resolution in MATLAB. *Chemometrics and Intelligent Laboratory Systems*, 76(1):101–110, 2005.

[31] Christian Julien, Alain Mauger, Karim Zaghib, and Henri Groult. Optimization of layered cathode materials for lithium-ion batteries. *Materials*, 9(595), 2016.

[32] K. C. Kam, A. Mehta, J. T. Heron, and M. M. Doeff. Electrochemical and Physical Properties of Ti-Substituted Layered Nickel Manganese Cobalt Oxide (NMC) Cathode Materials. *Journal of the Electrochemical Society*, 159(8):A1383–A1392, 2012.

[33] Arkady A. Karyakin. Prussian blue and its analogues: Electrochemistry and analytical applications. *Electroanalysis*, 13(10):813–819, 2001.

[34] Imanol Landa-Medrano, Andrea Sorrentino, Lorenzo Stievano, Idoia Ruiz de Larramendi, Eva Pereiro, Luis Lezama, Teofilo Rojo, and Dino Tonti. Architecture of Na-O2 battery deposits revealed by transmission X-ray microscopy. *Nano Energy*, 37:224–231, 2017.

[35] J. B. Leriche, S. Hamelet, J. Shu, M. Morcrette, C. Masquelier, G. Ouvrard, M. Zerrouki, P. Soudan, S. Belin, E. Elkaiim, and F. Baudelet. An Electrochemical Cell for Operando Study of Lithium Batteries Using Synchrotron Radiation. *Journal of The Electrochemical Society*, 157(5):A606, 2010.

[36] Michael A. Lilga, Rick J. Orth, Johanes P H Sukamto, Scot D. Rassat, J. David Genders, and Ram Gopal. Cesium separation using electrically switched ion exchange. *Separation and Purification Technology*, 24(3):451–466, 2001.

[37] Yuehe Lin and Xiaoli Cui. Electrosynthesis, characterization, and application of novel hybrid materials based on carbon nanotube-polyaniline-nickel hexacyanoferrate nanocomposites. *Journal of Materials Chemistry*, 16(6):585, 2006.

[38] M. S. Whittingham. Lithium Batteries and Cathode Materials. *Chemical Reviews*, 104(10):4271–4301, 2004.

[39] D L Massart, B G M Vandeginste, L M C Buydens, S De Jong, P J Lewi, J B T Data Handling in Science Smeyers-Verbeke, and Technology, editors. *Handbook of Chemometrics and Qualimetrics: Part A*, volume 20. Elsevier, 1998.

[40] K. Mizushima, J. B. Goodenough, P. C. Jones, and P. J. Wiseman. LixCoO2: A new cathode material for batteries of high energy density. *Materials Research Bulletin*, 15(6):783–789, 1980.

[41] Barbara Louise Mojet, Sune Dalgaard Ebbesen, and Leon Lefferts. Light at the interface: The potential of attenuated total reflection infrared spectroscopy for understanding heterogeneous catalysis in water. *Chemical Society Reviews*, 39(12):4643–4655, 2010.

[42] Angelo Mullaliu, Giuliana Aquilanti, Paolo Conti, Jasper R Plaisier, Marcus Fehse, Lorenzo Stievano, and Marco Giorgetti. Copper Electroactivity in Prussian Blue-Based Cathode Disclosed by Operando XAS. *The Journal of Physical Chemistry C*, 122(28):15868–15877, 7 2018.

[43] Angelo Mullaliu, Moulay T. Sougrati, Nicolas Louvain, Giuliana Aquilanti, Marie-Liesse Doublet, Lorenzo Stievano, and Marco Giorgetti. The electrochemical activity of the nitrosyl ligand in copper nitroprusside: a new possible redox mechanism for lithium battery electrode materials? *Electrochim. Acta*, 257:364–371, 12 2017.

[44] J W Niemantsverdriet. *Spectroscopy in Catalysis*. 2000.

[45] Y Nishi. Lithium ion secondary batteries; past 10 years and the future. *Journal of Power Sources*, 100(1-2):101–106, 2001.

[46] Daniel G Nocera and Nathan S. Lewis. Powering the planet: Chemical challenges in solar energy utilization. *Proc. Natl. Acad. Sci.*, 103(43):15729 –15735, 2006.

[47] PerkinElmer Life. FT-IR Spectroscopy. Attenuated Total Reflectance. Technical report, 2005.

[48] Daniel Pritzl, Sophie Solchenbach, Morten Wetjen, and Hubert A. Gasteiger. Analysis of Vinylene Carbonate (VC) as Additive in Graphite/LiNi 0.5 Mn 1.5 O 4 Cells. *Journal of The Electrochemical Society*, 164(12):A2625–A2635, 2017.

[49] W.E. Prout, E.R. Russell, and H.J. Groh. Ion exchange absorption of cesium by potassium hexacyanocobalt (II) ferrate (II). *Journal of Inorganic and Nuclear Chemistry*, 27(2):473–479, 1965.

[50] E. Reguera, J. F. Bertran, J. Miranda, and A. Dago. On the structure and Mossbauer spectra of ferrous nitroprusside. *Hyperfine Interactions*, 77:1–10, 1993.

[51] J. Rodríguez-Hernández, E. Reguera, and A. Gómez. Crystal structure of orthorhombic ferrous nitroprusside: Fe[Fe(CN)5NO].2H2O. *Powder Diffr.*, 20(01):27–32, 3 2005.

[52] C Ruckebusch and L Blanchet. Multivariate curve resolution: A review of advanced and tailored applications and challenges. *Analytica Chimica Acta*, 765:28–36, 2013.

[53] H. Shin, J. Park, A. M. Sastry, and W. Lu. Effects of Fluoroethylene Carbonate (FEC) on Anode and Cathode Interfaces at Elevated Temperatures. *Journal of the Electrochemical Society*, 162(9):A1683–A1692, 2015.

[54] Hai Shen Song, Zheng Cao, Zhi An Zhang, Yan Qing Lai, Jie Li, and Ye Xiang Liu. Effect of vinylene carbonate as electrolyte additive on cycling performance of LiFePO4/graphite cell at elevated temperature. *Transactions of Nonferrous Metals Society of China (English Edition)*, 24(3):723–728, 2014.

[55] Antonella Iadecola Stievano, Alexis Perea, Laurent Aldon, Giuliana Aquilanti, and Lorenzo. Li deinsertion mechanism and Jahn-Teller distortion in LiFe 0.75 Mn 0.25 PO 4 : an operando x-ray absorption spectroscopy investigation. *Journal of Physics D: Applied Physics*, 50(14):144004, 2017.

[56] J. M. Tarascon and M. Armand. Issues and challenges facing rechargeable lithium batteries. *Nature*, 414(6861):359–367, 2001.

[57] Mike Ware. Prussian Blue: Artists' Pigment and Chemists' Sponge. *Journal of Chemical Education*, 85(5):612–621, 2008.

List of Figures

1.1 Comparison between lithium-metal (a) and lithium-ion (b) batteries [56]. . 2

1.2 Volumetric and gravimetric energy density of the principle types of batteries [56]. 3

1.3 Main cathodic materials structures [38]. 6

1.4 Typical PBAs structure, with green A exchangeable counterions, light blue N, gray C, pink Fe and yellow M transition metal. 8

1.5 Mössbauer spectra and XRD patterns of hydrated (in the top in (a)) and dehydrated cubic Iron Nitroprusside. 10

2.1 Synthesized powders. 12

2.2 Coin cell structure. 15

2.3 Geometry of an *in situ* cell [35]. 16

3.1 Mössbauer spectrum of the degradation product of FeNP (Sample S1 (a)). 18

3.2 Registered Mössbauer spectrum of $Na_2[Fe(CN)_5NO] \cdot 2\,H_2O$. 19

3.3 Mössbauer spectrum of Sample 2(b) (FeNP). 20

3.4 Fit and XRD pattern of FeNP (Sample 2 (c)). 21

3.5 Temperature influence on crystals size in FeNP synthesis. 22

3.6 IR spectra of FeNP (sample S2 (b)), Fe(CN)O (sample S1 (a)) and of the nitroprusside precursor (noted R1). 23

3.7 Water characteristic peak in the three FeNP samples. 24

3.8 SEM image of Sample 2 (b) (FeNP) with indications on sampling points for EDX analysis. 24

3.9 SEM image of Sample 1 (b) with indications on some sampling points for EDX analysis. 27

3.10 SEM-EDX image of the degradation product in Sample 1 (b). Each color is representative for an element: yellow is for Fe, green for N, pink for S, light blue for O and red for C. 28
3.11 Galvanostatic cycles of FeNP in PTFE-based electrode. 29
3.12 Comparison between the three synthesized active materials: S2 (a) in AN064, S2 (b) in AN066 and S2 (c) in AN069. 30
3.13 Galvanostatic cycles of FeNP in CMC-based slurry. 31
3.14 Specific Capacity and Coulombic Efficiency trends for FeNP PTFE-based electrodes vs. Li metal. 32
3.15 Galvanostatic cycles of FeNP pellets against Sodium and Potassium. 33
3.16 Galvanostatic cycles and corresponding performances of Fe(CN)O pellets. . 33
3.17 Galvanostatic cycles and corresponding performances of Fe(CN)O in CMC-based slurry. 34
3.18 Galvanostatic cycles of Fe(CN)O pellets in Sodium and Potassium batteries. 35
3.19 Correlation between electrochemical cycle and XRD patterns registered for FeNP during the *in situ* XRD analysis. 36
3.20 *Operando* XRD patterns of FeNP. 36
3.21 FeNP XRD patterns from a frontal view. Each color correspond to a different diffractogram, from the pristine (dark blue) to the last one (dark red). 37
3.22 Correlation between electrochemical cycle and $_{57}$Fe Mössbauer spectra registered for Fe(CN)O during the *operando* analysis. 38
3.23 *Operando* $_{57}$Fe Mössbauer spectra of Fe(CN)O during cycling vs. Li. 39
3.24 Results of the PCA analysis of the full dataset of *operando* 40
3.25 Pure spectral components obtained from the MCR-ALS analysis of the *operando* Mössbauer data and evolution of their concentration during cycling. 40
3.26 Fitting of the pure components obtained from the MCR-ALS analysis of the *operando* Mössbquer spectra. 41

A.1 Diffraction angle according to the Bragg's equation. Figure taken from [21]. 46
A.2 Scheme of a diffractometer taken from [21] 47
A.3 C, H, N, S elemental analyzer with gas chromatograph and thermal conductivity detector [26]. 50

A.4 ATR-FTIR principle [41]. 51

List of Tables

1.1 Properties of principle ions for batteries. 4

3.1 Mössbauer parameters of the new photodegradation product, FeNP and the reactant NaNP. 18

3.2 WDX and EDX data for Fe(CN)O (measured on sample S1 (a)). 23

3.3 EDX results for FeNP (Sample 2 (b)) in the sampling points indicated in Figure 3.8 25

3.4 FeNP EXD and WDX results for each synthesized batch. 26

3.5 FeNP elementary analysis results. 26

3.6 FeNP (S1 (b)) WDX and EDX results. 27

3.7 ^{57}Fe Mössbauer hyperfine parameters of the pure components obtained from the MCR-ALS analysis of the *operando* Mössbquer spectra. 41